Monitoring the geologic storage of carbon dioxide using multi-component SAR interferometry

Alessio Rucci[1], D. W. Vasco[2], and Fabrizio Novali[1]

[1] *Tele Rilevamento Europa, Milano, Italy*

[2] *Berkeley Laboratory, University of California, Berkeley, California 94720*

SUMMARY

Combining interferometric synthetic aperture radar (InSAR) data from ascending and descending orbits we estimate both quasi-vertical and quasi-east-west displacements for a region in central Algeria, an area encompassing an active large-scale carbon dioxide storage project, the In Salah gas storage project. The surface deformation associated with the injection into three horizontal wells is clearly visible in the InSAR estimates. We find that the addition of the quasi-horizontal displacement data enables us to discriminate between source models producing similar vertical displacements. In particular, predictions from a model consisting of a distribution of volume changes restricted to the reservoir depth interval satisfies the quasi-vertical data but does not match the quasi-east-west displacement data. However, aperture changes on sub-vertical damage zones, intersecting each of the injection wells, give rise to displacements matching both the quasi-east-west and vertical components. In all cases we can match the observations with the most significant volume and aperture changes in regions immediately surrounding the injection wells.

Key words: Interferometry, deformation, inverse problem

1 INTRODUCTION

Long term monitoring is a key component of the geologic storage of carbon dioxide. This is particularly true during the initial development of storage technology, when the post-injection behavior of the carbon dioxide has only been documented in a few field studies (Arts et al. 2004, White et al. 2004). Geodetic methods, in particular techniques measuring surface deformation, can provide a basis for cost-effective long term reservoir surveillance. (Fielding et al. 1998, Vasco et al. 2000, Stancliffe et al. 2001, Schmidt and Burgmann 2003, Vasco and Ferretti 2005). Currently, there are a variety of available techniques, ranging from borehole emplaced tiltmeters (Evans et al. 1998, Palmer 1990, Castillo et al. 1997, Wright 1998, Wright et al. 1998) to satellite-based synthetic aperture radar systems (SAR) (Burgmann et al. 2000).

Two ways to improve the resolution of surface geodetic data are to improve spatial coverage and to include additional components of displacement. Dense spatial coverage allows one to estimate the shorter wavelength components of the deformation field. The inclusion of horizontal components allows for the discrimination between various source models producing the same vertical deformation (Dieterich and Decker 1975, Wright et al. 2004). Thus, it is desirable to maintain a high spatial sampling while providing multiple components of displacement. Satellite-based techniques, such as interferometric synthetic aperture radar (InSAR) provide dense spatial coverage (Hansson 2000). Multiple components of surface displacement may be derived from InSAR observations using amplitude correlations, as in Fialko et al. (2001a, 2005), or by combining data from various orbital geometries (Joughin et al. 1998, Fujiwara et al. 2000, Wright et al. 2004, Funning et al. 2005, Teatini et al. 2011). There have also been attempts to construct vertical and horizontal displacements from line-of-sight InSAR observations (e.g. Oppliger et al. 2006). However, the latter technique relies on rather restrictive assumptions, such as a volume source. In this paper we implement an approach advocated by Fujiwara et al. (2000), Wright et al. (2004), and Teatini et al. (2011), combining the SAR data stacks acquired from different satellite orbits. Because of the near polar nature of the Envisat orbits, we can only estimate two components (quasi-east-west and quasi-vertical) of displacement.

The decomposition into quasi-east-west and quasi-vertical components is applied to InSAR range change observations gathered at the In Salah carbon dioxide gas storage project in central Algeria. The In Salah storage project is one of a handful of industrial-scale carbon sequestration efforts in the world (Ringrose et al. 2009, Mathieson et al. 2010). Interferometric synthetic aperture radar (InSAR) data is used to monitor the fate of the carbon dioxide after it is injected into a geologic formation at a depth of roughly two kilometers. One goal of this study is to verify that incorporating the horizontal component does indeed allow us to further discriminate between possible source models. A secondary

goal is to determine if it is possible to fit the two components of data with a model containing the most significant changes near the injection wells.

2 METHODOLOGY

Here we discuss the technique used to estimate the quasi-vertical and quasi-east-west displacement components. We also briefly outline our inversion methodology, in which we use the two components to estimate subsurface volume and aperture changes due to the injection of carbon dioxide.

2.1 A Two-dimensional displacement decomposition

Synthetic aperture radar observations obtained from a single orbit simply measure the projection of the surface displacement along the line-of-sight from the satellite to a reflection point on the Earth's surface (Massonnet and Feigl 1998, Burgmann et al. 2000, Wright et al. 2004). However, it is feasible to combine observations obtained from both ascending and descending orbits to approximate quasi-vertical and quasi-east-west components of motion. To see this, consider a Cartesian coordinate system where the X axis is oriented in the easterly direction, the Y axis points to the north, and the Z axis is directed upward. In general, in the coordinate system (X,Y,Z) the displacement, $\mathbf{U}$, of a scatterer on the Earth's surface is represented as the sum

$$\mathbf{U} = U_x\mathbf{s}_x + U_y\mathbf{s}_y + U_z\mathbf{s}_z \tag{1}$$

where U_x, U_y, and U_z are the components of $\mathbf{U}$ in the east, north, and vertical directions, and $\mathbf{s}_x$, $\mathbf{s}_y$, and $\mathbf{s}_z$ are the unit vectors in the respective directions (Hanssen 2001).

In this paper we use range change data from two distinct geometries, associated with ascending and descending satellite orbits. Given estimates of range change from two orbital geometries we have the projections of a particular vector displacement onto two line-of-sight vectors. Using only two projections it is generally not possible to derive the full three-dimensional displacement vector. However, due to the almost polar orbital geometry, the direction cosine in the northerly direction is small (Joughin et al. 1998, Fujiwara et al. 2000, Teatini et al. 2011). Specifically, the track only deviates 7° from a north-south orientation and the look-vector is dominantly in the easterly direction. Thus, the projections onto the look vectors associated with each orbit, $\mathbf{a}$ and $\mathbf{b}$, are

$$U_a = \mathbf{U} \cdot \mathbf{a} \approx U_x a_x + U_z a_z \tag{2}$$

$$U_b = \mathbf{U} \cdot \mathbf{b} \approx U_x b_x + U_z b_z, \tag{3}$$

two equations for U_x and U_z. We shall frequently refer to the quantities U_x and U_z as the quasi-east-west and quasi-vertical components, respectively.

The two equations (2) and (3) are well-posed if the angle between the line-of-sight and the vertical is sufficiently large. That is, we can solve the equations if the look vector of the satellite is not close to the vertical. A more formal measure of our ability to estimate the quasi-east-west and quasi-vertical components from the ascending and descending orbit vectors in provided by their covariances. A compact formal expression for the covariance matrix follows if we write equations (2) and (3) in matrix form:

$$\boldsymbol{\rho} = \mathbf{AU}$$

where

$$\mathbf{A} = \begin{pmatrix} a_x & a_z \\ b_x & b_z \end{pmatrix}$$

and

$$\boldsymbol{\rho} = \begin{pmatrix} U_a \\ U_b \end{pmatrix}.$$

Because the governing equation is linear, we can relate the covariance matrix associated with the original ascending and descending range change measurements, $\mathbf{C}_\rho$ to the covariance matrix associated with the quasi-east-west and quasi-vertical estimates, $\mathbf{C}_x$:

$$\mathbf{C}_x = \mathbf{A}^{-1}\mathbf{C}_\rho(A^{-1})^T$$

(Parker 1994). The specific elements of the covariance matrix $\mathbf{C}_x$ depend upon the covariance matrix of the range change estimates and upon the geometry of the two orbits, as measured by the elements of the matrix $\mathbf{A}$.

2.2 Estimation of volume change and aperture change

Here we outline the methodology used to relate surface deformation to processes at depth. The approach is guided by the field case described below: the injection of supercritical carbon dioxide into a thin, deep reservoir. Various aspects of this approach have been presented elsewhere (Vasco et al. 2008, Rucci et al. 2010, Vasco et al. 2010). For example, it was noted in Vasco et al. (2008) and Vasco et al. (2010), that there are indications of volumetric change along a narrow corridor within the reservoir, extending northwest and southeast from the injection wells (Vasco et al. 2008). Furthermore, a double-lobed pattern observed over one of the wells suggested the opening of a tensile feature, such as a fault or fracture (Vasco et al. 2010). Here we generalize the previous approaches by allowing for

volume change within the sub-horizontal reservoir and for both aperture changes and volume changes within a sub-vertical fault/fracture zone.

We consider the situation in which we attribute the surface deformation to the injection of a large volume of supercritical carbon dioxide into the reservoir. The injected fluid induces pressure changes, leading to volume expansion within the reservoir and possibly fault or fracture growth. Due to spatial variations in the hydrological properties, the flow and pressure changes at depth may be controlled by heterogeneity. Furthermore, as noted by Rucci et al. (2010), the geomechanical properties may also vary spatially, and the resulting fluid pressure changes can lead to varying amounts of reservoir volume change. Therefore, we shall allow for spatially-varying volume expansion and aperture changes within the designated source regions.

There are two end-member models to consider: flow and volume change confined to the reservoir interval and flow primarily within a sub-vertical damage zone. As an aside, we note that we also tried a third composite model in which aperture change on a damage zone was combined with volume change within the reservoir. We found that volume change confined to the reservoir level was not able to compensate for aperture changes a hundred meters or more above the reservoir. Such a combination resulted in a depression in the surface displacement above the damage zone (Vasco et al. 2000), something not observed in some areas, such as above well KB-503. Thus, in order to obtain surface displacements similar to what we observed at In Salah, it was necessary to include models that had variable amounts of volume change and aperture change at, and above, the depth of the reservoir. In the following sub-sections we describe each of the end-member models.

2.2.1 Reservoir Volume Change

The first model invokes fluid flow and pressure changes confined to the reservoir interval. The reservoir is modeled as a single layer undergoing spatially-varying volume expansion due to the injected carbon dioxide and the accompanying pressure changes. Spatially variability is allowed in order to account for heterogeneity in both flow properties and geomechanical attributes. As described in previous publications (Vasco et al. 1988, Vasco et al. 2000, Rucci et al. 2010), when the overburden behaves elastically we may formulate the relationship between the displacement vectors, $\mathbf{u}_z$ (quasi-east-west) and $\mathbf{u}_v$ (vertical) respectively, and the volume changes in the grid blocks $\mathbf{v}$ as

$$\begin{aligned} \mathbf{u}_h &= \mathbf{G}_h \mathbf{v} \\ \mathbf{u}_z &= \mathbf{G}_z \mathbf{v} \\ \mathbf{v} &\geq \mathbf{0} \end{aligned} \tag{4}$$

where $\mathbf{G}_h$ and $\mathbf{G}_z$ are the horizontal and vertical Green's functions, determined by the nature of the medium in which the reservoir lies (Vasco et al. 1988). In what follows we shall use the Green's functions for a layered elastic medium (Wang and Kuempel 2003, Wang et al. 2006). The layered model that we used is the same as the elastic model plotted in Vasco et al. (2010). For the forward problem we have the model parameters, the reservoir volume changes $\mathbf{v}$, and we compute the surface displacements $\mathbf{u}_h$ and $\mathbf{u}_z$. For the inverse problem we use the observed surface displacements to infer the distribution of volume change within the reservoir.

As in Rucci et al. (2010), we employ the reflective Newton's method of Coleman and Li (1996) to solve the inverse problem. We solve the system (4) in a least squares sense, reformulating the problem as the minimization of a quadratic function subject to inequality constraints. The inverse problem is typically ill-posed and often does not have a unique solution (Savage et al. 1980, Parker 1994). In such cases we introduce additional constraints in the form of quadratic penalty functions that are added to the function to be minimized (Du et al. 1992, Parker 1994, Murray et al. 2001, Pritchard et al. 2002, Fialko 2004). As in Rucci et al. (2010) the penalty terms used here include a measure of model roughness, and a distance measure penalizing changes far from the injection point. The distance penalty corresponds to the assumption that the largest volume and aperture changes should occur at, or near, the injection point. Thus, we minimize the penalized least squared function

$$P = W_e \parallel \mathbf{u} - \mathbf{Gt} \parallel_2 + W_r \parallel \mathbf{St} \parallel_2 + W_d \parallel \mathbf{Dt} \parallel_2 \tag{5}$$

where $\parallel \mathbf{v} \parallel_2$ signifies the L_2 norm of the vector $\mathbf{v}$ (Parker 1994), W_e is the data weighting, W_r is the roughness penalty term weighting, $\mathbf{S}$ is a roughness operator, a finite-difference approximation to the spatial gradient, W_d is the distance weighting, $\mathbf{D}$ is a distance matrix with elements of $||\mathbf{x}_j - \mathbf{x}_i||$ on the diagonal, where $\mathbf{x}_j$ is the location of the center of the grid block and $\mathbf{x}_i$ is the location of the injection well.

2.2.2 Damage zone aperture and volume change

While it was expected that the injected carbon dioxide would remain within the sandstone reservoir, there are indications that one or more vertical or sub-vertical damage zones may have acted as conduits for flow of the injected fluid (Vasco et al. 2010). Specifically, a double lobed pattern, visible in the InSAR images above the injector KB-502 (Vasco et al. 2010), suggests the opening of a tensile feature at depth. Furthermore, elongated patterns of uplift over the other injectors implies the existence of narrow northwest trending high permeability features controlling the flow. For example, the deformation pattern over the well KB-501 is reminiscent of volume change in a narrow region that may reflect a fault or a fracture zone (Vasco et al. 2008). Furthermore, recent seismic results image a nar-

row, 100-300 m thick, zone intersecting well KB-502 and KB-503, co-located with, and sub-parallel to, the InSAR anomaly (Gibson-Poole and Raikes 2010). Based upon these considerations, we have adopted a composite damage zone model in which both tensile dislocations (fault/fracture opening) and volume expansion may occur in a narrow planar zone. Our motivation for adopting a composite model containing both volume and aperture change is the suggestion in the pattern of surface deformation that both mechanisms may be at play. In particular, the double-lobed pattern over well KB-501 suggests a damage zone model with aperture change. Conversely, the simple uplift pattern over well KB-503 suggests that the deformation is largely generated by volume expansion. These two mechanisms may operate in the damage zone along with any volume expansion within the reservoir layer caused by the injection of the carbon dioxide.

The composite damage zone model is similar to models used to simulate dike intrusion (Fialko et al. 2001b, Segall 2010). The relationship between the quasi-vertical displacement ($\mathbf{u}_z$), the quasi-east-west displacement ($\mathbf{u}_h$), and the damage zone volume changes $\mathbf{v}$ and tensile dislocations $\mathbf{t}$ is written mathematically as

$$\begin{aligned} \mathbf{u}_h &= \mathbf{G}_h\mathbf{v} + \mathbf{T}_h\mathbf{t} \\ \mathbf{u}_z &= \mathbf{G}_z\mathbf{v} + \mathbf{T}_z\mathbf{t} \\ \mathbf{v} &\geq \mathbf{0} \\ \mathbf{t} &\geq \mathbf{0} \end{aligned} \tag{6}$$

assuming that the region surrounding the reservoir and the damage zone behaves elastically. The sensitivity matrices $\mathbf{G}_h$ and $\mathbf{G}_z$ are similar to those given above, $\mathbf{T}_h$ and $\mathbf{T}_z$ are sensitivity matrices corresponding to the aperture change associated with tensile dislocations, such as the opening of a fracture (Wang et al. 2006). We also impose a restriction that the volume change is proportional to the opening of the dislocation

$$\mathbf{v} = k\mathbf{t}. \tag{7}$$

We invoke the constraint (7) because we expect that in regions where the opening of the damage zone is large, in particular near the injection well, the volume change will also be the large. The constraint reduces the non-uniqueness associated with the inverse problem. As the dislocation and volume sources are related by the expression (7), we can rewrite the system of equations (6) as

$$\begin{aligned} \mathbf{u}_h &= (k\mathbf{G}_h + \mathbf{T}_h)\,\mathbf{t} \\ \mathbf{u}_z &= (k\mathbf{G}_z + \mathbf{T}_z)\,\mathbf{t} \\ \mathbf{t} &\geq \mathbf{0}. \end{aligned} \tag{8}$$

Note that, through the last inequality, we require fracture opening and associated fractional volume increase, due to the injection of the carbon dioxide. Also note that one can combine the effects of volume change within the reservoir, equations (4), with the effects of volume change and aperture change within the damage zone, equations (8). As in Rucci et al. (2010), we solve the system of equations (8) for $\mathbf{t}$ in a least squares sense using the reflective Newton's method of Coleman and Li (1996). The data constraints (8) are augmented by the penalty terms described above [see equation (5)], and the augmented system of equations is solved.

3 APPLICATION: THE GEOLOGIC STORAGE OF CARBON DIOXIDE AT IN SALAH, ALGERIA

3.1 Overview and previous work at the storage site

The In Salah storage project is one of earliest industrial-scale carbon sequestration efforts (Ringrose et al. 2009, Mathieson et al. 2010), along with the Weyburn (White et al. 2004) and Sleipner (Arts et al. 2004) projects. The project, located in central Algeria (Figure 1), involves removing excess carbon dioxide from natural gas produced at three adjacent gas fields. The extracted carbon dioxide is compressed and injected on the flanks of an anticline defining one of the nearby gas fields, the Krechba field. The carbon dioxide gas is returned to the original reservoir layer, a roughly 20 meter thick sandstone lying at a depth of approximately 1.8 kilometers. At this depth the carbon dioxide is in a supercritical state and even though it is a liquid it has properties akin to those of a gas. The three horizontal injection wells, KB-501, KB-502, and KB-503, are indicated in Figures 1 and 2. The thin reservoir layer is overlain by approximately a kilometer of mudstones and shales, forming a sealing cap. Another kilometer of interbedded sandstone and shale lies above the shale cap. The injection has continued since 2004 and several million metric tonnes of carbon dioxide have been sequestered in this fashion (Ringrose et al. 2009, Mathieson et al. 2010).

In an effort to monitor the fate of the sequestered carbon dioxide, interferometric synthetic aperture radar (InSAR) data was used to observe surface displacement above the wells during the period of injection. As indicated in the radar image in Figure 1, the Earth's surface above the injectors is characterized by hard rock and boulder strewn fields, with little mobile sand, and thus nearly ideal for InSAR monitoring. The main difficulties are provided by several dry river beds or wadii's and by a seasonal lake bed to the north of well KB-503 (Figure 1).

In two previous studies, Vasco et al. (2008) and Vasco et al. (2010), a single component of line-of-sight displacement, the range change, was used to infer flow-related deformation at depth. The temporal progression of surface deformation, and by inference the volume change in the reservoir,

suggests fluid migration along a narrow high-permeability, northwest trending, conduit within the reservoir at well KB-501 (Vasco et al. 2008). A later analysis of the double lobed pattern in range change over the injection well KB-502 to the north, (see Figure 2a), suggests the opening of a tensile feature (Vasco et. al. 2010). The In Salah project has an active monitoring program (Mathieson et al. 2010) and InSAR is just one aspect of the surveillance and verification. As noted above, data from seismic surveys has supported the notion of two vertical north-west trending damage zones intersecting the wells KB-502 and KB-503 (Gibson-Poole and Raikes 2010). However, no such seismic data is available in the region surrounding KB-501.

3.2 Estimation of vertical and horizontal displacement

The data are comprised of ascending and descending radar phase measurements from the Envisat archive of the European Space Agency (ESA). The temporal baseline associated with the data is from July 2004 to May 2008. For the ascending geometry the normal baseline is 500 m while for the descending geometry the baseline is 270 m. We compensate for the effects of topography using the SRTM elevation model (Hanssen 2000, p. 13). In order to correct for orbital errors we estimate and remove planes for both the ascending and descending geometries. A variogram is used to capture the statistical characteristics of the atmospheric noise (Hanssen 2000). The noise power and the spatial correlation length are estimated for each image used in the analysis.

Using the technique noted in the Methodology section, we map the ascending and descending orbit range change data to estimates of quasi-vertical and quasi-east-west displacement. As noted by Fujiwara et al. (2000), Wright et al. (2004) and Teatini et al. (2011) the near polar orbit, with an azimuth near 7°, means that the range change is relatively insensitive to northerly motion. Using equations (2) and (3), we can solve the system for U_x and U_z, the quasi-east-west and the vertical displacements. We use pairs of ascending and descending images from July of 2004 and May of 2008. Because only two sets of ascending images are available for processing, it is not possible to apply multi-interferogram techniques for atmospheric noise removal (Ferretti et al. 2001). However, using the full set of descending interferograms, which provide a time series, we performed a statistical analysis of the atmospheric noise power in the area surrounding the In Salah injections. In a region excluding the area of active deformation we constructed a variogram in order to capture the statistical characteristics of the atmospheric noise for both components of displacement. From this analysis we estimate the covariance matrix of the range change estimates

$$\mathbf{C}_\rho = \begin{pmatrix} 6.25 & 0.00 \\ 0.00 & 6.25 \end{pmatrix}$$

where the the components are in squared millimeters. From the parameters for the ascending and descending orbits, that is the vectors for the ascending (0.3290, 0.9415, -0.0733) and the descending (-0.3865, 0.9189, -0.0786) geometries, we can form the matrix $\mathbf{A}$:

$$\mathbf{A} = \begin{pmatrix} 0.3290 & 0.9415 \\ -0.3685 & 0.9189 \end{pmatrix}$$

and use above formula for the a posteori covariance matrix, $\mathbf{C}_x = \mathbf{A}^{-1}\mathbf{C}_\rho(A^{-1})^T$, to arrive at standard error estimates of 0.5 cm and 0.2 cm for the eastwest and vertical displacements, respectively. The standard error estimates for the two components agree with the analysis of Wright et al. (2004) and Teatini et al. (2011). Specifically, these studies found that the quasi-vertical standard errors are roughly one-half of the quasi-east-west standard errors.

The resulting vertical and horizontal displacement components are shown in Figure 2 for the region surrounding the three injection wells. Note the uplift of about 2 cm above each of the injectors, in agreement with previous range change estimates (Vasco et al. 2008, Vasco et al. 2010). Away from the injection wells there are vertical variations due to atmospheric effects and near surface changes, such as seasonal displacement in the dried riverbeds or wadii's, of around 0.5 cm. Away from the wadii's the vertical displacement error appears to be smaller, in the range of 0.25 cm, in general agreement with the above statistical analysis. The horizontal displacements are roughly the same magnitude as the vertical displacements. However, the level of horizontal motion in areas far from the injectors seems of the order of 0.5 cm or so, roughly twice as high for the vertical component. These error estimates are roughly half of those given in the studies of Wright et al. (2004) and Teatini et al. (2011) associated with the Envisat satellites. They give relative errors for the horizontal and vertical components as 1.0 cm and 0.5 cm, respectively. The smaller errors may be due to the favorable surface characteristics at the In Salah, a mostly boulder strewn hard surface. In addition, the desert climate may have less moisture variation then the studies of Wright et al. (2004) and Teatini et al. (2011), which focused on a volcano in Alaska and a river valley, respectively.

3.3 Analysis of the displacements above well KB-501

In this sub-section we consider the horizontal and vertical displacements from a region immediately surrounding injection well KB-501, located on the eastern flank of the anticline that defines the In Salah field (Figure 1). As a first step we use the two components of displacement to infer volumetric expansion solely within the reservoir layer (Figure 3). That is, we assume that the surface displacement is due entirely to the injected carbon dioxide migrating throughout the reservoir. The injected fluid leads to pressure and volume changes within the reservoir formation, stress changes in the re-

gion surrounding the reservoir, and deformation within the overburden. We allow for variable volume change within the reservoir layer, dividing the layer into a 20 by 20 grid of cells, where each cell is 400 m by 400m in extent and 20 m thick. Each cell may undergo distinct volume change and the relationship between volume change and surface deformation is given by the system of constraints (4). We solve this system of equations subject to the bounds

$$\mathbf{v} \geq \mathbf{0} \tag{9}$$

using the method of Coleman and Li (1996). Before minimizing P we need to choose appropriate values for the weights W_e, W_r, and W_d in the penalty function (5). For the data weights W_e we use the inverse of the standard errors of the observations. We kept the roughness penalty weighting W_r at a very small value as compared to the other weights. We chose the distance weight W_d by trial and error. That is, we conducted several inversions and examined the fit to the observations and the compactness of the solution. When the data fit was deemed acceptable, within the estimated errors, we took that value for W_d.

The volume changes within the reservoir layer, resulting from an inversion of the data in the region around KB-501, are shown in Figure 3. The peak volume change is located at the injection well and the region of volume change is oriented along a northwest trending corridor. The fits to both the horizontal and vertical components of displacement are shown in Figure 4. For a perfect match the calculated displacement would equal the observed displacement and the points would lie on the dashed diagonal line plotted in Figure 4. The calculated vertical component of displacement, plotted in red, seems to match the observations within the estimated error of 0.25 cm. However, the calculated horizontal component appears to be systematically lower in magnitude when compared with the observed values, with deviations exceeding the estimated error of 0.50 cm. Thus, it appears that predictions based upon a model containing volume change solely within the reservoir do match the observed vertical displacements but do not match the observed horizontal displacements.

Next, in an attempt to improve the fit to the horizontal components of displacement, we adopt the damage zone model discussed above [see equation (8)]. In this model a vertical or sub-vertical damage zone can undergo both tensile opening, which we refer to as aperture change, and volume expansion. The model parameters, the location and the dip of the planar damage zone, were found using a grid search for a reduced set of model parameters: a damage zone model consisting of only four patches. As in the more detailed model, each of the four patches could undergo volume expansion and aperture change. The location and the dip were systematically varied on a grid. The best-fitting dip is 83° and the best-fitting location is indicated in Figure 2b by the dashed white line intersecting well KB-501. Due to the imposed proportionality between aperture and volume change, as expressed in equation (7),

we solve for a single, spatially-varying quantity. The relative ratio, expressed by the proportionality constant k in equation (7), was found in the initial grid search, discussed above. For the inversion at well KB-501, k is given by 0.015.

After we estimate the damage zone geometry, we use the surface deformation to estimate the aperture changes, $\mathbf{t}$ and fractional volume changes, $\mathbf{v}$ distributed over the region. The width of the damage zone was taken to be 100 m. Note that some care is required in the inversion because the damage zone model is vertical or sub-vertical and the various parts of the model can lie at significantly different depths. For surface displacements the sensitivity to aperture and volume changes can vary strongly with depth, leading to instability in the inverse problem. For example, in Figure 5 we plot the results of an inversion for the tensile opening distributed over a plane that varies from 0.8 to 2.4 km in depth. For this inversion we implemented a more commonly used norm penalty term in the regularization of the inverse problem:

$$P = W_e \parallel \mathbf{u} - \mathbf{G}\mathbf{t} \parallel_2 + W_n \parallel \mathbf{t} \parallel_2 \tag{10}$$

where W_n is the model norm penalty weighting. Because the sensitivity of surface displacement data to a dislocation within the Earth is a strong function of depth, the observations are most strongly influenced by the aperture and volume changes closest to the surface. Therefore, conventional regularization penalties, such as a norm penalty, can potentially biases the result to favor shallow aperture changes. This effect is seen in Figure 5, where the solution contains small shallow aperture changes and deeper and larger aperture change but little change near the injection well. This solution fits the observations as well as the model that we derive using the regularization (5), pointing to the inherent non-uniqueness associated with the inverse problem.

In general, it would seem that the model in Figure 5, with the largest aperture changes hundreds of meters away from the injection well and randomly distributed shallow aperture change, is not the most physically plausible model. Rather, given the continuous injection of carbon dioxide over several years, we would expect that, baring some heterogeneous distribution of mechanical properties, the largest aperture and volume changes should lie near the injection point. Therefore, we impose a penalty for aperture and volume changes that increases with distance from the injection point. Including this penalty term and eliminating the norm penalty results in the solution for aperture change and volume expansion shown in Figure 6a. This solution is in accordance with a physically reasonable distribution of pressure surrounding the injection well, with largest changes at the injector and values decreasing as a function of the distance from the well. In cases where the spatial variations of geomechanical properties do result in the largest changes at some distance from the well, for example as in Rucci

et al. (2010), the least squares minimization of the penalized misfit does allow for aperture/volume changes away from the well if they are indeed required to fit the observations.

There appears to be preferential flow to the northwest of the well KB-501, to the left in Figure 6a. This agrees with the inversion for reservoir volume change, shown in Figure 3, where the volume change extends to the northwest of the injection well. A similar result was obtained from an earlier inversion for reservoir volume change as a function of time (Vasco et al. 2008). The aperture change also appears to be asymmetric in depth, skewed towards shallower depths. This might reflect density variations in injected carbon dioxide, which is less dense then the in situ pore fluid. We should also emphasize that we are estimating aperture and volume changes that are likely to be strongly influenced by fluid pressure variations. Thus, the changes are reflective of fluid pressure increases, subject to variations in geomechanical properties, and do not necessarily indicate where the carbon dioxide has migrated.

Using the Monte carlo based approach described in Rucci et al. (2010) we computed the standard errors associated with our model parameter estimates (Figure 6b). The data error estimates of 0.25 and 0.50 cm for the quasi-vertical and quasi-east-west displacement components are used in the calculation of the standard errors. The magnitude of the model parameter errors is roughly 12 % of the peak aperture change (Figure 6a). The largest errors are near the injection well and extend along the reservoir layer. The errors are influenced by the data distribution, the data uncertainty, the regularization, and the Green's function. The distance weighting in the regularization may explain why the peak errors are found close to the injection well. The layered velocity structure, with a low velocity layer surrounding the reservoir and a high velocity layer just below the reservoir, may explain why larger errors are found at or below the reservoir depth and elongated in the horizontal direction. In Vasco et al. (2010) the layered velocity structure and the large variations in elastic properties were found to have a significant impact on the surface deformation. The layered Green's function and the depth variations in sensitivities due to the layering may also explain why the norm constrained inversion (Figure 5) has the largest aperture change just below the reservoir.

Figure 7 plots the predicted displacement against the observed displacement for the horizontal and vertical components. Now both of the calculated components appear to match the observations. There is considerably more scatter in the horizontal component than there is in the vertical component, in agreement with the analysis of Wright et al. (2004) and Teatini et al. (2011), and the general variations seen in Figure 2. That is, in Figure 2 we noted the greater variation in the horizontal component away from the injection wells where we do not expect to see deformation, suggesting a larger error in that component.

Figure 8 displays the averaging kernel associated with a dislocation estimate at the injector, de-

noted by the star in the figure. The averaging kernel, computed by the techniques described in Rucci et al. (2010), accounts for the positivity constraints in the system of equations (7). In addition, model roughness and distance weighting penalties are used to regularize the solution. The averaging length is roughly 300 to 400 meters, elongated along the length of the damage zone. Thus, we should not interpret features in our solutions that are finer then this length.

3.4 Analysis of the displacements above wells KB-502 and KB-503

The vertical and horizontal displacements above wells KB-502 and KB-503 indicate that the injection of carbon dioxide gives rise to surface deformation. While there appears to be some separation between vertical uplift over each well (Figure 2a), it seems that the horizontal displacements interfere (Figure 2b). In particular, the anti-symmetric pattern of east-west displacement due to radial displacement away from the source, is seen over wells KB-501 and KB-502 but is not clear over well KB-503. Specifically, significant eastward motion is not seen to the east of well KB-503. To account for this interference, we conduct a simultaneous inversion for tensile dislocations and volume changes on two damage zones. As in the case of the analysis at well KB-501 described above, we use a grid search to estimate the locations (shown in Figure 2b) and the dip angle of the damage zones, roughly 85°. In Figure 2 we can see that one damage zone intersects well KB-502 while the other is sub-parallel and intersects well KB-503. In the grid search we also solve for the values of k for the damage zones intersecting wells KB-502 and KB-503 [see equation (6)], producing values of 0.14 and 0.009, respectively.

Due to the coupled nature of the surface deformation in the region between the two wells, we must solve for aperture changes on the two damage zones simultaneously. In Figure 9a we show the aperture changes for the zone intersecting well KB-502. The aperture changes, indicating overall damage zone opening are shown in this figure. The result is similar to that for KB-501, indicating pressure migration to the northwest (to the left in the figure). Also, the asymmetry in depth is evident, with the most significant aperture change found at or above the reservoir interval. These features were also present in an inversion of range change for aperture change in a vertical fracture and volume change in the reservoir interval (Vasco et al. 2010). However, changes in Figure 9a do extend slightly shallower, to a depth of about 1.5 to 1.6 km. The peak change is slightly to the northwest of the injection point, perhaps due to noise in the data, there is a wadii cutting across the anomaly above well KB-502 (Figures 1 and 2). The offset in peak aperture and volume change could also be due to variations in geomechanical properties (Rucci et al. 2010), that is, the damage zone could be more compliant to the north. The standard deviations associated with the estimates are shown in Figure 9b. The peak model parameter error values are around 5 cm, much smaller then the peak estimated

aperture changes of 35 cm. As in the error estimates shown in Figure 6b, the peak errors are found at or below the reservoir depth interval, perhaps indicating the influence of the layered elastic model (Vasco et al. 2010).

The opening associated with the injection at KB-503 is shown in Figure 10a. The dislocation indicates pressure migration to the south-east (to the right) of the injection well. The pattern is in accordance with the vertical displacement in Figure 2, indicating that the area of uplift extends to the south-east of the injection well KB-503. The standard errors, shown in Figure 10b, are less then 10% of the peak aperture changes of 2.5 cm. The distribution of errors is similar to that seen in Figures 6b and 9b, with the largest errors at or below the reservoir interval.

In Figure 11a and 11b the predicted vertical and horizontal displacement components are shown for all three wells. The calculated displacements are in fair agreement with the measured deformation, plotted in Figure 2a and 2b. The residuals associated with the observed horizontal and vertical displacements over the wells are shown in Figure 12. The predicted displacements are due to aperture and volume changes on both damage zones. In general the vertical and horizontal displacement residuals lie within their expected errors. However, the models appear to under-predict the largest negative (westward) horizontal displacements. This may be due to noise in the data because in Figure 2 one observes negative values extending far west of the well KB-503. Alternatively, heterogeneity may play a role because the damage zone is likely to have very different properties from the average layer properties used in our modeling. There may be some migration of fluid within the reservoir itself, away from the damage zone.

Considering the results given above, we see that the size of the tensile dislocation can vary dramatically. For example, the peak tensile opening at well KB-503, about 3 cm, is more than an order of magnitude smaller than the 40 cm of opening estimated for well KB-502, . The implication is that flow out of well KB-502 mainly leads to aperture changes distributed over a higher permeability damage zone, whereas, for the flow out of well KB-503 leads to a strong volumetric expansion. Such considerations are supported by the vertical displacements plotted in Figure 2a. In particular, the deformation above well KB-502 is primarily characterized by a double-lobed pattern of uplift, typical for a tensile feature at depth. The pattern over well KB-503, a single peak of uplift centered over the damage zone, is suggestive of volume change at depth.

4 CONCLUSIONS

As shown here, the inclusion of the horizontal component of displacement adds useful information. In particular, it allows us to discriminate between a model comprised of a layer of distributed volume changes and a vertical damage zone model incorporating fault/fracture aperture changes and

fault/fracture volume change. The value of the horizontal components of displacement has already been demonstrated in the numerical simulations of Dieterich and Decker (1975) and our results support their conclusions. More recently, Wright et al. (2004) have shown how the incorporation of horizontal components reduced the trade-offs in a Monte-Carolo inversion of InSAR data for the fault parameters of the Nenana Mountain Earthquake in Alaska. With the addition of new satellites, such as Cosmos-Skymed and Terrasar-X, it will be possible to extract horizontal components in a routine fashion.

Finding a unique model is difficult with surface geodetic data, even when two components of displacement are available. In this study, in the face of such non-uniqueness, we were most interested in answering two questions. Firstly, could we fit the observations with volume changes solely within the reservoir interval? Secondly, can one fit the observations with volume/aperture changes distributed on a sub-vertical fault/fracture (damage zone) immediately surrounding the injection well? All results with distributed properties, including those in published fault dislocation models are strongly influenced by the regularization, be it imposed explicitly, as in our distance weighting, or implicitly through a norm constraint coupled with the strong depth dependence of the Green's functions. The results of our study indicate the importance of damage zones in controlling the flow of injected carbon dioxide. That is, using just a sub-vertical composite fault/fracture model we can match the overall vertical and horizontal displacements (compare Figures 2 and 11). By adding minor flow within the reservoir we should be able to improve the match somewhat.

While we are able to match the observed surface displacements with aperture and volume changes near the injection wells, this does not mean that the carbon dioxide must remain in this region. There is the issue of non-uniqueness, other solutions exist that are compatible the data. It is possible to find solutions with shallower aperture and volume changes that can explain the observations. Furthermore, as noted earlier, aperture and volume changes most likely reflect the total fluid pressure changes and do not necessarily correspond to fluid saturation changes. The carbon dioxide is influenced by density variations and may possibly migrate upward by buoyancy. Such migration may not involve the large pressure changes associated with the fluid injection at the wells. Additional monitoring, such as time-lapse seismic imaging or electromagnetic sounding, will be required in order to constrain the changes in carbon dioxide saturation over time. Also, coupled modeling can help in determining if the solutions are compatible with the physical processes that are thought to control the migration of the injected carbon dioxide (Rutqvist et al. 2010, Bissell et al. 2011, Gemmer et al. 2012, Rutqvist 2012).

ACKNOWLEDGMENTS

Work performed at Lawrence Berkeley National Laboratory and Tele-Rilevamento Europa (TRE) was

supported by the US Department of Energy under contract number DE-AC02-05 CH11231, Office of Basic Energy Sciences, and the GEOSEQ project for the Assistant Secretary for Fossil Energy, Office of Coal and Power Systems, through the National Energy Technology Laboratory of the US Department of Energy. The In Salah CO_2 Joint Industry Project (BP, Statoil, and Sonatrach) is thanked for the provision and interpretation of injection and subsurface data. Work performed at Tele-Rilevamento Europa (TRE) was supported by BP and LBNL.

REFERENCES

Arts, R., O. Eiken, R. A. Chadwick, P. Zweigel, L. Van der Meer, and B. Zinszner, 2004, Monitoring of CO_2 injected at Sleipner using time-lapse seismic data, *Energy*, **29**, 1383-1392.

Bissell, R. C., Vasco, D. W., Atbi, M., Hamdani, M., Okwelegbe, M., and Goldwater, M. H., 2011, A full field simulation of the In Salah gas production and CO_2 storage project using a coupled geo-mechanical and thermal fluid flow simulator, *Energy Procedia*, **4**, 3290-3297.

Burgmann, R., R. A. Rosen, and E. J. Fielding, 2000, Synthetic aperture radar interferometry to measure Earth's surface topography and its deformation, *Annual Reviews of Earth and Planetary Sciences*, **28**, 169-209.

Castillo, W., S. Hunter, P. Harben, C. Wright, R. Conant, and E. Davis, 1997, Deep hydraulic fracture imaging: Recent advances in tiltmeter technologies, *International Journal of Rock Mechanics and Mining Science*, **34** , 3-4.

Coleman, T.F. and Y. Li, 1996, A Reflective Newton Method for Minimizing a Quadratic Function Subject to Bounds on Some of the Variables, *SIAM Journal on Optimization*, **6**, 1040-1058.

Dieterich, J. H., and Decker, R. W., 1975. Finite element modeling of surface deformation associated with volcanism, *Journal of Geophysical Research*, **80** , 4094-4102.

Du, Y., Aydin, A., and Segall, P., 1992. Comparison of various inversion techniques as applied to the determination of a geophysical deformation model for the 1983 Borah Peak earthquake, *Bulletin of the Seismological Society of America*, **82** , 1840-1866.

Evans, K. F., G. R. Holzhausen, and M. D. Wood, 1982, The geometry of a large-scale nitrogen gas hydraulic fracture formed in Devonian shale: An example of fracture mapping using tiltmeters, *Society of Petroleum Engineers Journal*, **22**, 755-763.

Ferretti, A., Prati, C, and Rocca, F., 2001, Permanent scatterers in SAR interferometry, *Institute of Electrical and Electronics Engineers Transactions on Geoscience and Remote Sensing*, **39** , 8-20.

Fialko, Y., 2004. Probing the mechanical properties of seismically active crust with space geodesy: Study of the co-seismic deformation due to the 1992 M_w 7.3 Landers (Southern California) earthquake, *Journal of Geophysical Research*, **109**, doi:10.1029/2003JB002756.

Fialko, Y., Simons, M., and Agnew, D., 2001a, The complete (3-D) surface displacement field in the epicentral area of the 1999 M_w 7.1 Hector Mine earthquake, California, from space geodetic observations, *Geophysical Research Letters*, **37**, doi:10.1029/2009GL041544, 1-5.

Fialko, Y., Khazan, Y., and Simons, M., 2001b, Deformation due to a pressurized horizontal circular crack in a elastic half-space, with applications to volcano geodesy *Geophysical Journal International*, **146**, 181-190.

Fialko, Y., Sandwell, D., Simons, M., and Rosen, P., 2005, Three-dimensional deformation caused by the Bam, Iran, earthquake and the origin of shallow slip deficit, *Nature*, **435**, doi:10.1038/nature03425, 295-299.

Fielding, E. J., R. G. Blom, and R. M. Goldstein, 1998, Rapid subsidence over oil fields measured by SAR interferometry: *Geophysical Research Letters*, **25**, 3215-3218.

Fujiwara, S., Nishimura, T., Murakami, M., Nakagawa, H., Tobita, M., and Rosen, P. A., 2000, 2.5-D surface deformation of M6.1 earthquake near Mt. Iwate detected by SAR interferometry, *Geophysical Research*

Letters, **27**, 2049-2052.

Funning, G. J., Parsons, B., Wright, T. J., Jackson, J. A., and Fielding, E. J., 2005. Surface displacements and source parameters of the 2003 Bam (Iran) earthquake from Envisat advanced synthetic aperture radar imagery, *Journal of Geophysical Research*, **110** , B09406, doi:10.1029/2004JB003338.

Gemmer, L., Hansen, O., Iding, M., Leary, S., and Ringrose, P., 2012, Geomechanical response to CO_2 injection at Krechba, In Salah, Algeria, *First Break*, **30**, 79-84.

Gibson-Poole, C. M. and Raikes, S., 2010. Enhanced understanding of CO_2 storage at Krechba from 3D seismic, *Proceedings of the 9th Annual Conference on Carbon Capture and Sequestration*, Pittsburgh, Pennsylvania, May 10-13, 2010.

Hanssen, R. F., 2001, *Radar Interferometry*, Kluwer Academic Publishers, Dordrecht.

Joughin, I. R., Kwok, R., and Fahnestock, M. A., 1998, Interferometric estimation of three-dimensional ice-flow using ascending and descending passes, *Institute of Electrical and Electronics Engineers Transactions on Geoscience and Remote Sensing*, **36** , 25-37.

Massonnet, D., and Feigl, K. L., 1998, Radar interferometry and its application to changes in the earth's surface *Reviews of Geophysics*, **36**, 441-500.

Mathieson, A., Midgley, J., Dodds, K., and Wright, I., 2010, CO_2 sequestration monitoring and verification technologies applied at Krechba, Algeria, *The Leading Edge*, **29**, 216-222.

Murray, J. R., Segall, P., Cervelli, P., Prescott, W., and Svarc, J., 2001. Inversion of GPS data for spatially variable slip-rate of the San Andreas Fault near Parkfield, CA, *Geophysical Research Letters*, **28**, 359-362.

Oppliger, G., Coolbaugh, M., and Shevenell, L., 2006. Improved visualization of satellite radar InSAR observed structural controls at producing geothermal fields using modeled horizontal surface displacements, *Geothermal Research Council Transactions*, **30** , 927-930.

Palmer, I. D., 1990, Uplifts and tilts at Earth's surface induced by pressure transients from hydraulic fractures, *Society of Petroleum Engineers Production Engineering*, **5**, 324-332.

Parker, R. L., 1994, *Geophysical Inverse Theory*, Princeton University Pressure, Princeton.

Pritchard, M. E., Simons, M., Rosen, P. A., Hensley, S., and Webb, F. H., 2002. Co-seismic slip from the 1995 July 30 M_w=8.1 Antofagasta, Chile, earthquake as constrained by InSAR and GPS observations, *Geophysical Journal International*, **150**, 362-376.

Ringrose, P., Atbi, M., Mason, D., Espinassous, M., Myhrer, O., Iding, M., Mathieson, A., and Wright, I., 2009, Plume development around well KB-502 at the In Salah CO_2 storage site, *First Break*, **27**, 1-5.

Rucci, A., Vasco, D. W., and F. Novali, 2010, Fluid pressure arrival-time tomography: Estimation and assessment in the presence of inequality constraints with an application to production at the Krechba field, Algeria, *Geophysics*, **75**, O39-O55.

Rutqvist, J., 2012, The geomechanics of CO_2 storage in deep sedimentary formations, *Geotechnical and Geological Engineering*, , doi 10.1007/s10706-011-9491-0.

Rutqvist, J., Vasco, D. W., and Myer, L., 2010, Coupled reservoir-geomechanical analysis of CO_2 injection and ground deformation at In Salah, Algeria, *International Journal of Greenhouse Gas Control*, **4**, 225-230.

Segall, P., 2010, *Earthquake and volcano deformation*, Princeton University Press, Princeton.

Savage, J. C., Lisowski, M., and Prescott, W. H., 1980. An apparent shear zone trending North-Northwest across the Mojave Desert into Owens Valley, Eastern California, *Geophysical Research Letters*, **17**, 2113-2116.

Schmidt, D. A., and R. Burgmann, 2003, Time-dependent land uplift and subsidence in the Santa Clara valley, California, from a large interferometric synthetic aperture radar data set, *Journal of Geophysical Research*, **108**, doi:10.1029/20002JB002267,4-1/4-13.

Stancliffe, R. P. W., and M. W. A. van der Kooij, 2001, The use of satellite-based radar interferometry to monitor production activity at the Cold Lake heavy oil field, Alberta, Canada, *American Association of Petroleum Geologists Bulletin*, **85**, 781-793.

Teatini, P., N. Castelletto, M. Ferronato, G. Gambolati, C. Janna, E. Cairo, D. Marzorati, D. Colombo, A. Ferretti, A. Bagliani, F. Bottazzi, 2011, Geomechanical response to seasonal gas storage in depleted reservoirs: A case study in the Po River basin, Italy, *Journal of Geophysical Research*, **116**, 1-21.

Vasco, D. W., L. R. Johnson, and N. Goldstein, 1988, Using surface deformation and strain observations to determine deformation at depth, with an application to Long Valley Caldera, California, *Journal of Geophysical Research*, **93** , 3232-3242.

Vasco, D. W., K. Karasaki, and C. Doughty, 2000, Using surface deformation to image reservoir dynamics, *Geophysics*, 65 , 132-147.

Vasco, D. W., A. Ferretti, and Novali, 2008, Estimating permeability from quasi-static deformation: Temporal variations and arrival-time inversion, *Geophysics*, **73**, O37-O52.

Vasco, D. W., Rucci, A., Ferretti, A., Novali, F., Bissell, R., Ringrose, P., Mathieson, A., and Wright I., 2010. Satellite-based measurements of surface deformation reveal fluid flow associated with the geological storage of carbon dioxide, *Geophysical Research Letters*, **37**, doi:10.1029/2009GL041544, 1-5.

Vasco, D. W., and A. Ferretti, 2005, On the use of quasi-static deformation to understand reservoir fluid flow, *Geophysics*, **70**, O13-O27.

Wang, R., and H.-J., Kuempel, 2003, Poroelasticity: Efficient modeling of strongly coupled, slow deformation processes in a multilayered half-space, *Geophysics*, **68**, 705-717.

Wang, R., F. Lorenzo-Martin, and F. Roth, 2006, PSGRN/PSCMP-a new code for calculating co- and post-seismic deformation, geoid and gravity changes based on the viscoelastic-gravitational dislocation theory, *Computers and Geosciences* **32**, 527-541.

White, D. J., G. Burrowes, T. Davis, Z. Hajnal, K. Hirsche, I. Hutcheon, E. Majer, B. Rostron, and S. Whittaker, 2004, Greenhouse gas sequestration in abandoned oil reservoirs: The International Energy Agency Weyburn pilot project, *GSA Today*, **14**, 4-10.

Wright, C. A., 1998, Tiltmeter fracture mapping: From the surface and now downhole, *Petro. Eng. Int.*, January, 50-63.

Wright, C. A., E. J. Davis, W. A. Minner, J. F. Ward, L. Weijers, E. J. Schell, and S. P. Hunter, 1998, Surface tiltmeter fracture mapping reaches new depths - 10,000 feet and beyond?, *Society of Petroleum Engineers*, **39919**, April.

Wright, T. J., Parsons, B. E., and Lu, Zhong, 2004, Toward mapping surface deformation in three dimensions using InSAR, *Geophysical Research Letters*, **31**, doi:10.1029/2003GL018827, 1-5.

Figure 1. Radar image of the In Salah carbon dioxide storage site with the well locations of the three carbon dioxide injectors KB-501, KB-502, and KB-503 indicated by the black lines. The approximate location of the gas field is indicated by the red curve. The insert is a plot of the North African region. The location of the In Salah radar image within Algeria outlined by the dashed oval within the insert.

Figure 2. (a) Vertical displacement, in centimeters, between July 2004 and May 2008. Upward motion is positive (blue) and downward motion, or subsidence is negative (red). The thick black lines indicate the extent of each of the three horizontal wells (KB-501, KB-502, and KB-503) within the reservoir. The approximate location of the gas field is indicated by the thin black curve. (b) Horizontal displacement for the same time period. Eastward motion is positive (blue) while motion to the west is negative (red). As in Figure 2a, the horizontal extent of the injection wells is denoted by the thick solid black lines. The approximate location of the gas field is indicated by the thin black curve. The dashed white lines indicate the traces of the three damage zones used in the inversion of the displacement data.

Figure 3. The distribution of volume changes within the reservoir layer that best matches the vertical and horizontal InSAR displacement data in the vicinity of well KB-501. The trace of the horizontal injection well KB-501 is indicated by the solid Line. The volume change is required to be positive, in accordance with the injection of supercritical carbon dioxide into the layer.

Figure 4. The fit to the observed vertical (red open circles) and horizontal (blue stars) displacements in the vicinity of well KB-501. The predictions were made using the horizontal reservoir model shown in Figure 3. If there were ideal agreement between the observed and predicted data then all the points would lie upon the diagonal dashed line plotted on the figure.

Figure 5. The aperture change on a sub-vertical damage zone intersecting injection well KB-501, resulting from an inversion of the vertical and horizontal displacement data. In this inversion only the data misfit and a model norm penalty terms were included, as in equation (10). The 20 m thick reservoir layer is indicated by the parallel black lines. The intersection of the injection well KB-501 with the damage zone plane is indicated by the white star.

Figure 6. (a) Aperture change on a sub-vertical damage zone intersecting well KB-501, resulting from an inversion of the vertical and horizontal displacement data. For this inversion only a roughness penalty and a term penalizing aperture changes as a function of distance from the injection well were used in the regularization. (b) Standard errors associated with the estimated aperture changes shown in Figure 6a. The model parameter errors are estimated using the Monte Carlo approach described in Rucci et al. (2010). The reservoir interval is indicated by the parallel black lines and the well intersection is denoted by the white star.

Figure 7. The fit to the observed vertical (red open circles) and horizontal (blue stars) displacements. The predictions were made using the sub-vertical fracture model with the aperture changes shown in Figure 6a.

Figure 8. Averaging kernel for an estimate of the aperture change for the patch located at the injection point (indicated by the white star). The regularization for the inverse problem included both a model roughness penalty and a distance penalty [see the penalty function (5)].

Figure 9. (a) Aperture change on a sub-vertical damage zone intersecting well KB-502, resulting from an inversion of the vertical and horizontal displacement data. (b) The corresponding aperture change standard errors associated with the model parameter estimates shown in panel (a).

Figure 10. (a) Aperture change on a sub-vertical damage zone intersecting well KB-503, resulting from an inversion of the vertical and horizontal displacement data. (b) The corresponding aperture change standard errors associated with the model parameter estimates shown in panel (a).

Figure 11. (a) Predicted vertical displacements for the entire region shown in Figure 2a. The traces of the three injection wells are indicated by the thick black lines in the figures. The approximate location of the gas field is indicated by the thin black curve. (b) Predicted horizontal displacements for the entire region shown in Figure 2b.

Figure 12. (a) Residuals associated with the vertical displacements for the entire region shown in Figure 2a. The traces of the three injection wells are indicated by the black lines in the figures. (b) Residuals associated with the horizontal displacements for the entire region shown in Figure 2b. The white rectangles signify the sub-regions used in the two sets of inversions, one for the aperture change associated with well KB-501 and the other for the aperture change associated with wells KB-502 and KB-503.

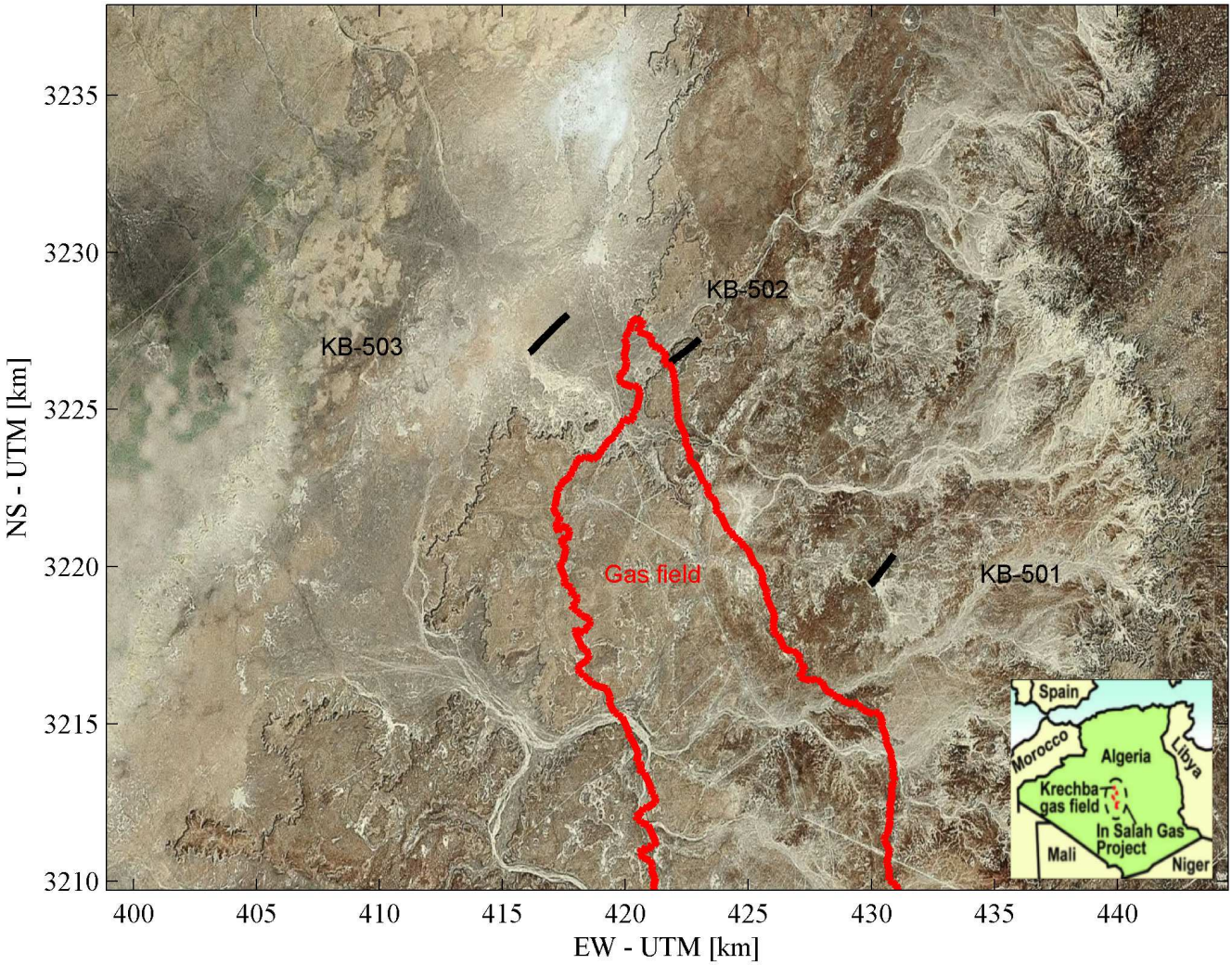
KB-503
KB-502
KB-501
Gas field
Spain
Morocco
Algeria
Libya
Krechba gas field
In Salah Gas Project
Mali
Niger
NS - UTM [km]
EW - UTM [km]
3235
3230
3225
3220
3215
3210
400
405
410
415
420
425
430
435
440

Figure 1.

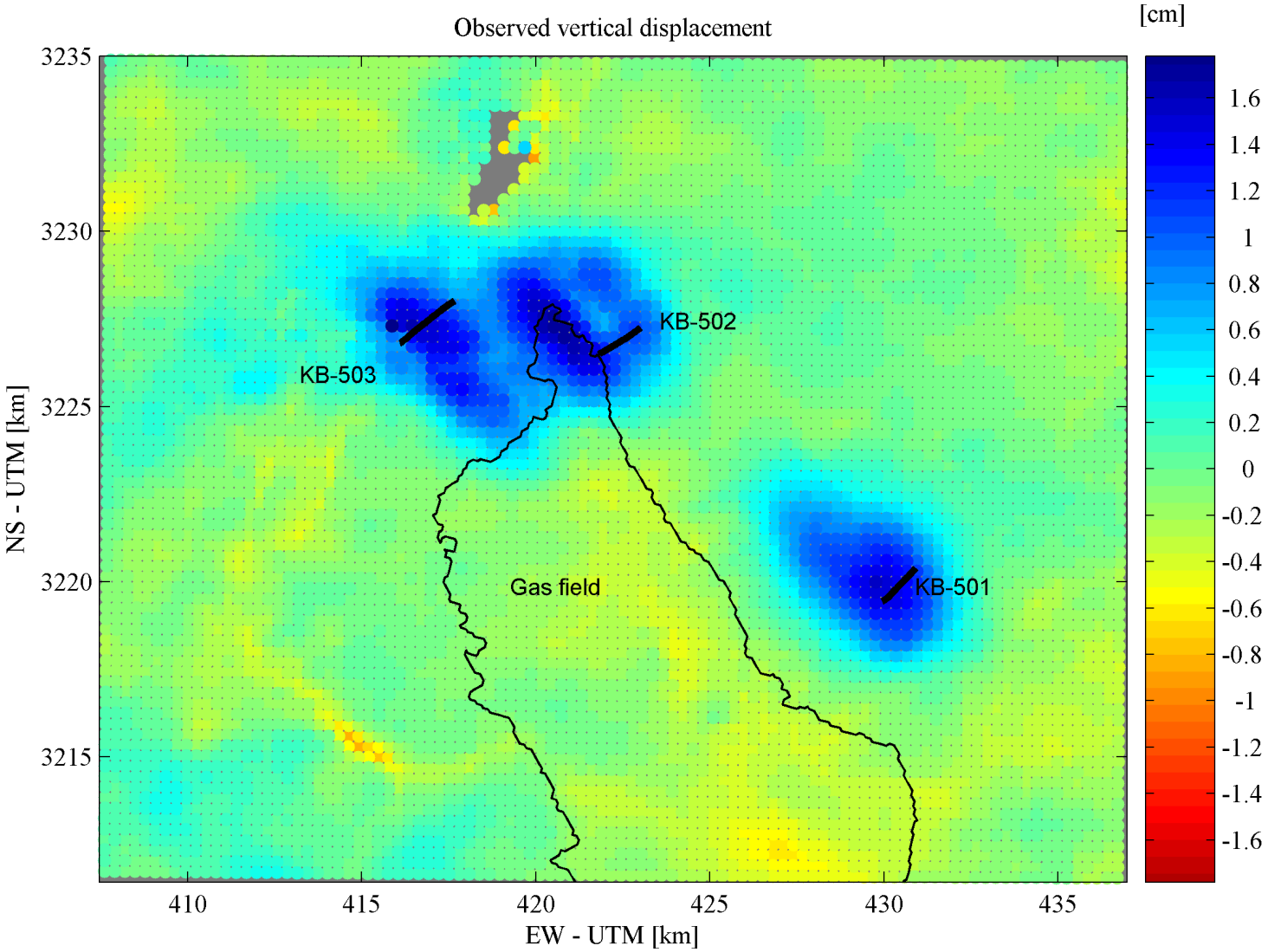
Observed vertical displacement
[cm]
3235
3230
3225
3220
3215
NS - UTM [km]
410
415
420
425
430
435
EW - UTM [km]
KB-503
KB-502
KB-501
Gas field
1.6
1.4
1.2
1
0.8
0.6
0.4
0.2
0
-0.2
-0.4
-0.6
-0.8
-1
-1.2
-1.4
-1.6

Figure 2a.

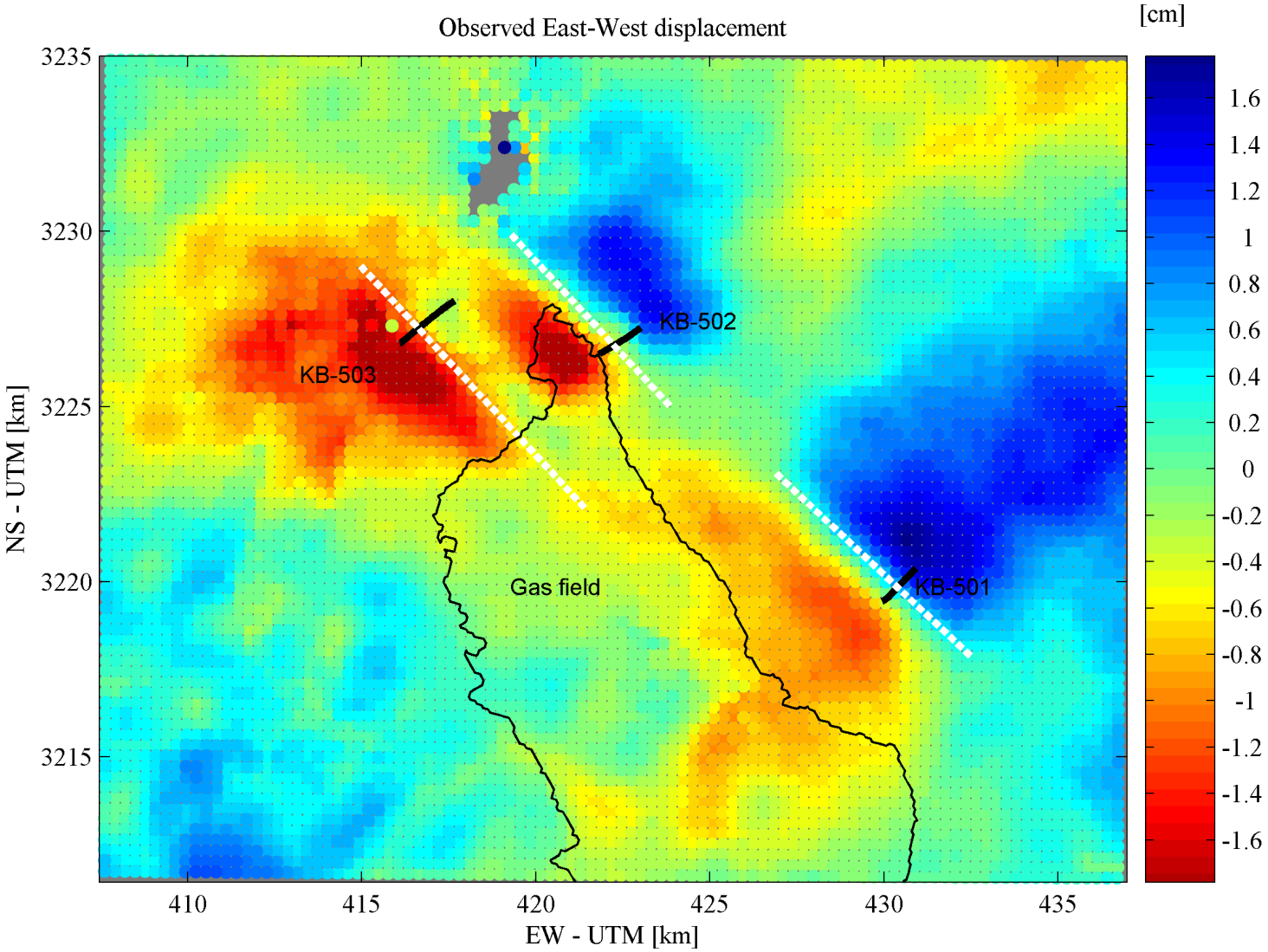
Observed East-West displacement
[cm]
3235
3230
3225
3220
3215
NS - UTM [km]
410
415
420
425
430
435
EW - UTM [km]
KB-503
KB-502
KB-501
Gas field
1.6
1.4
1.2
1
0.8
0.6
0.4
0.2
0
-0.2
-0.4
-0.6
-0.8
-1
-1.2
-1.4
-1.6

Figure 2b.

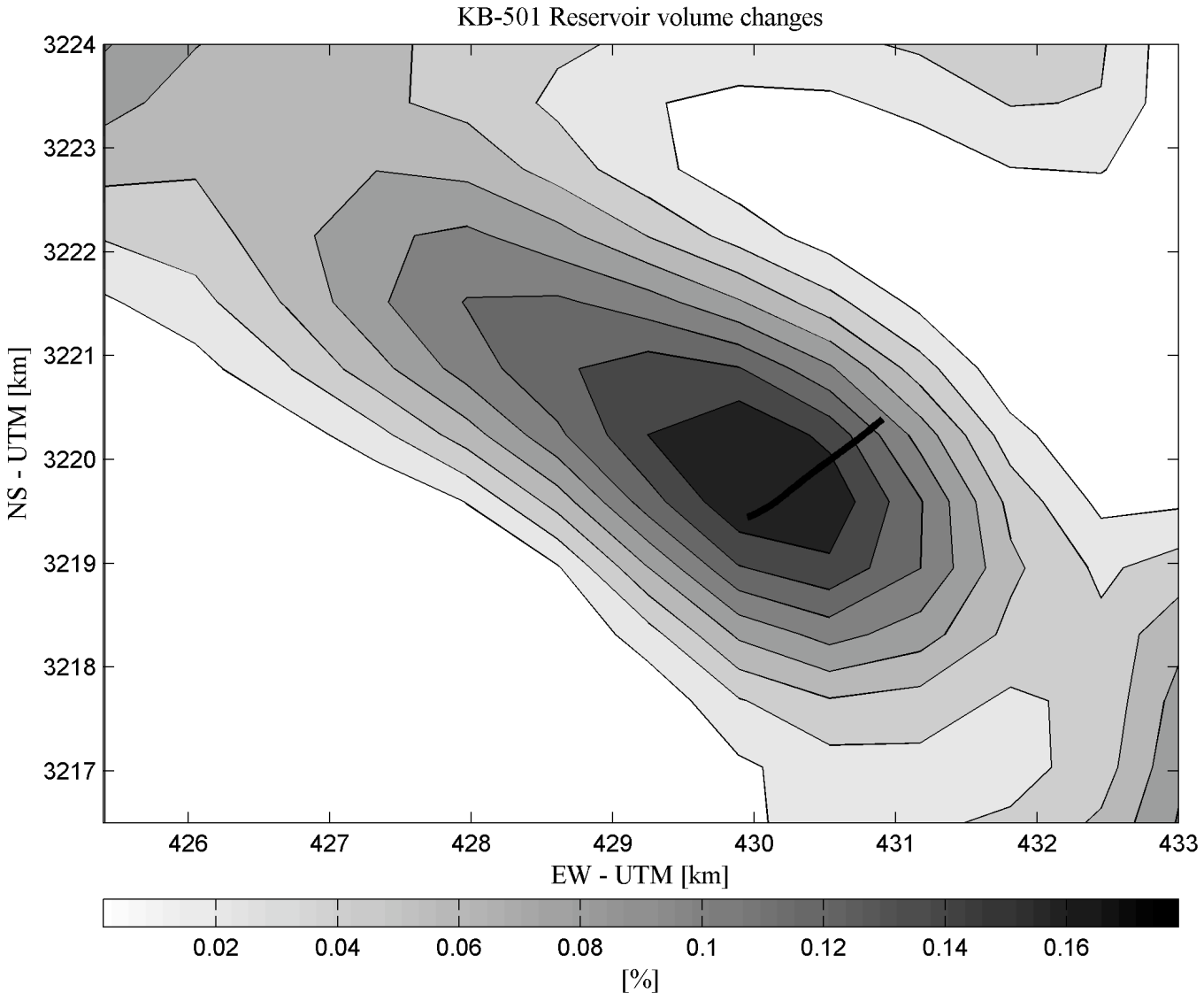
KB-501 Reservoir volume changes
3224
3223
3222
3221
3220
3219
3218
3217
NS - UTM [km]
426
427
428
429
430
431
432
433
EW - UTM [km]
0.02
0.04
0.06
0.08
0.1
0.12
0.14
0.16
[%]

Figure 3.

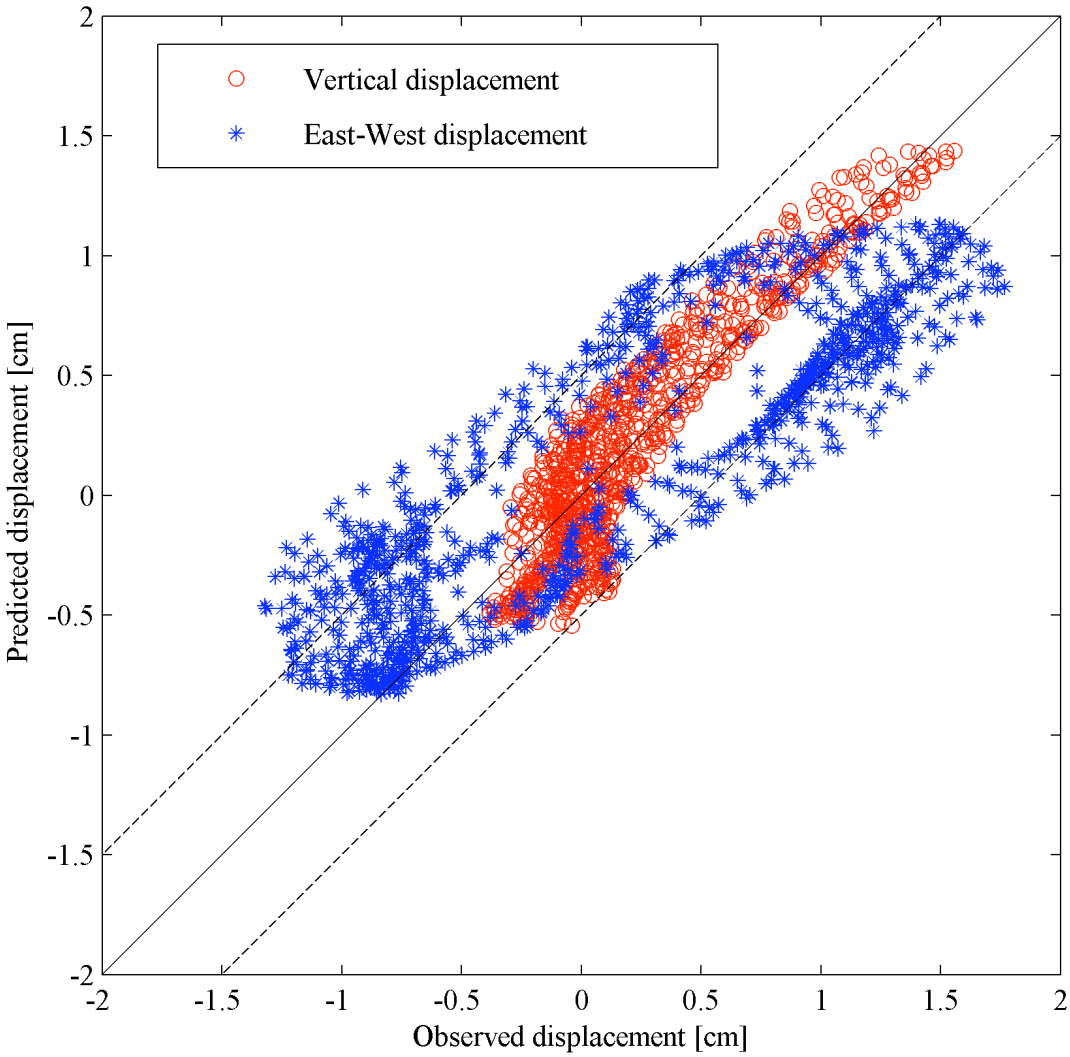
Vertical displacement
East-West displacement
Predicted displacement [cm]
Observed displacement [cm]
2
1.5
1
0.5
0
-0.5
-1
-1.5
-2
-2
-1.5
-1
-0.5
0
0.5
1
1.5
2

Figure 4.

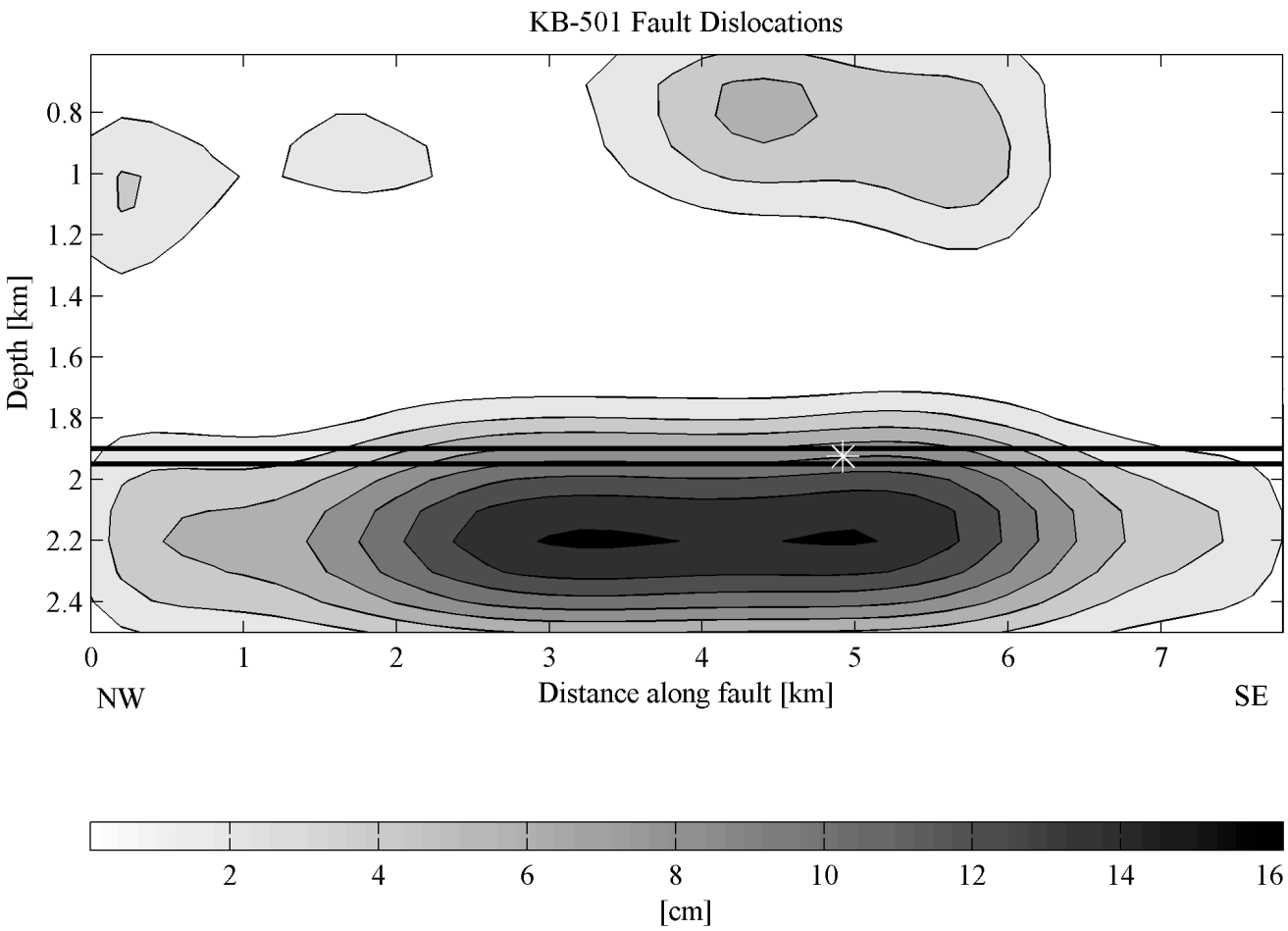
KB-501 Fault Dislocations
Depth [km]
0.8
1
1.2
1.4
1.6
1.8
2
2.2
2.4
0
1
2
3
4
5
6
7
NW
Distance along fault [km]
SE
2
4
6
8
10
12
14
16
[cm]

Figure 5.

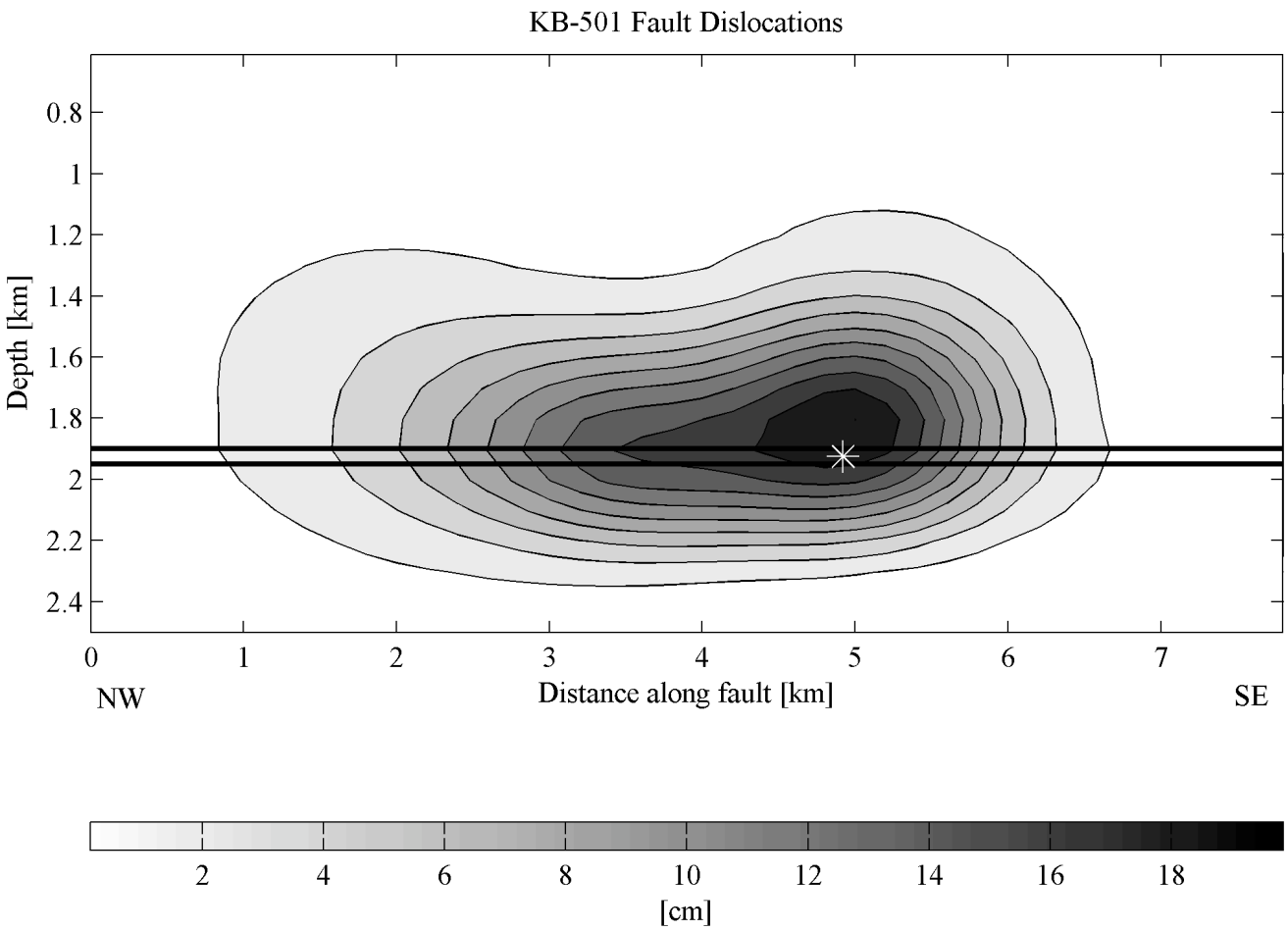
KB-501 Fault Dislocations
Depth [km]
0.8
1
1.2
1.4
1.6
1.8
2
2.2
2.4
0
1
2
3
4
5
6
7
NW
Distance along fault [km]
SE
2
4
6
8
10
12
14
16
18
[cm]

Figure 6a.

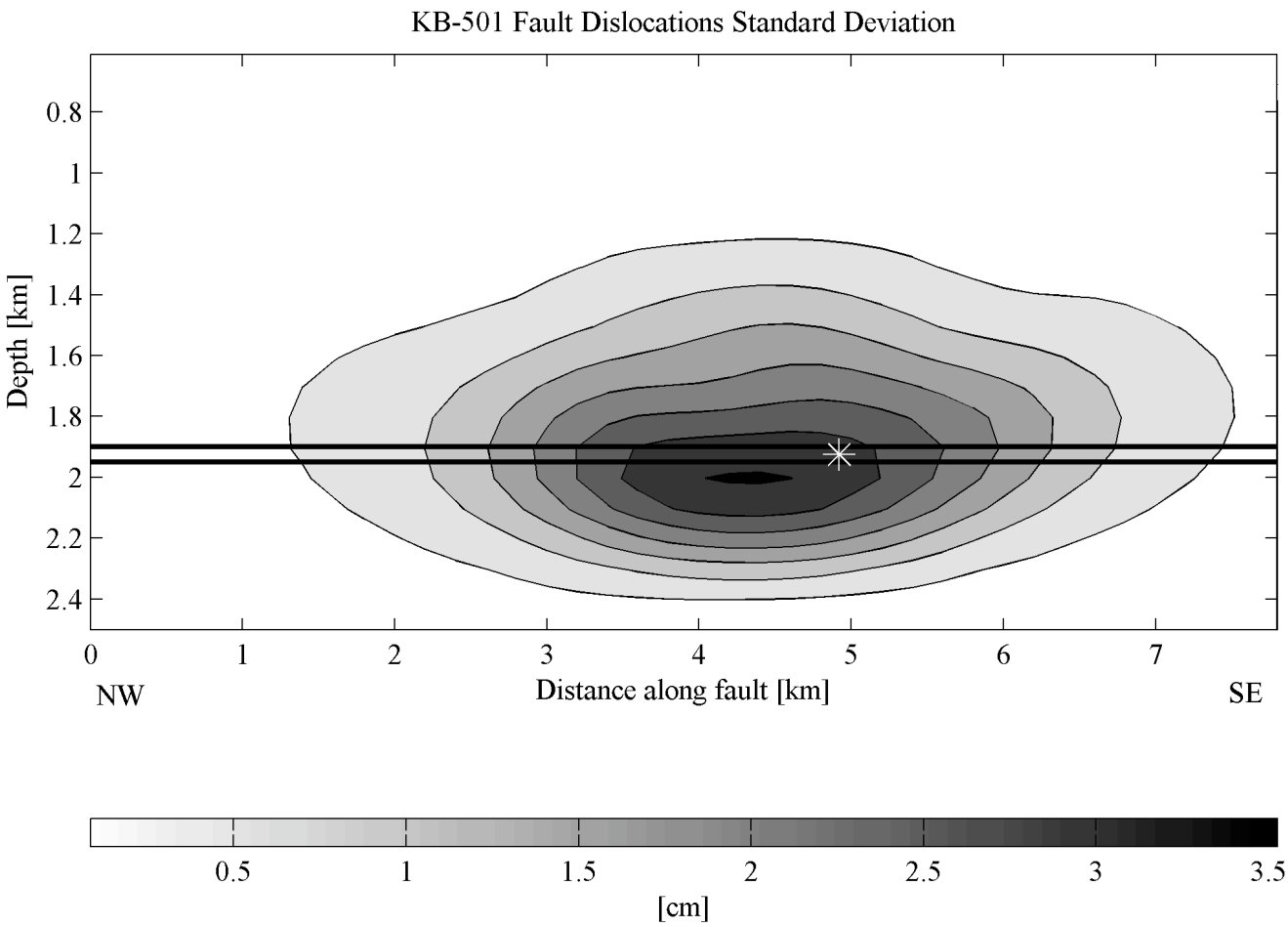
KB-501 Fault Dislocations Standard Deviation
Depth [km]
0.8
1
1.2
1.4
1.6
1.8
2
2.2
2.4
0
1
2
3
4
5
6
7
NW
Distance along fault [km]
SE
0.5
1
1.5
2
2.5
3
3.5
[cm]

Figure 6b.

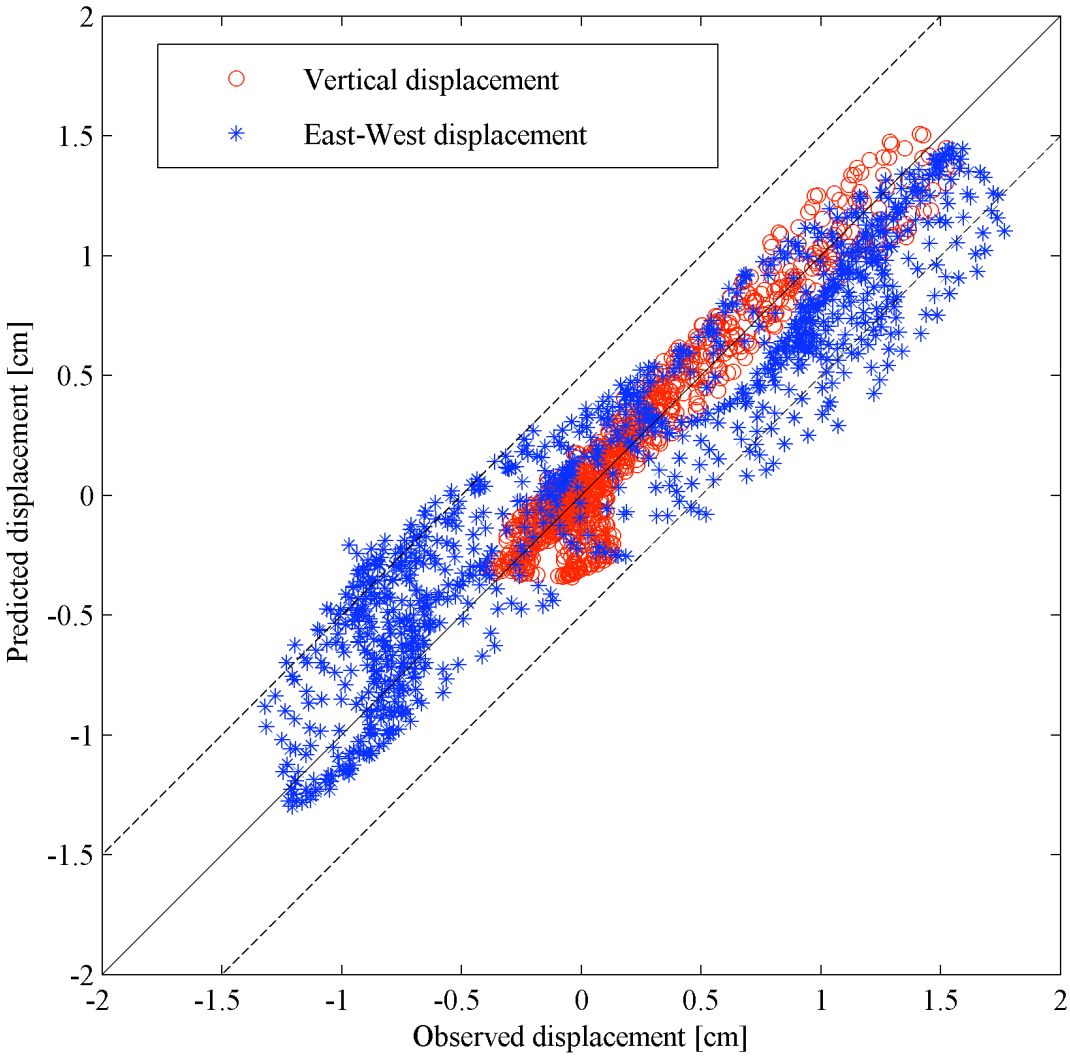
Vertical displacement
East-West displacement
Predicted displacement [cm]
Observed displacement [cm]
2
1.5
1
0.5
0
-0.5
-1
-1.5
-2
-2
-1.5
-1
-0.5
0
0.5
1
1.5
2

Figure 7.

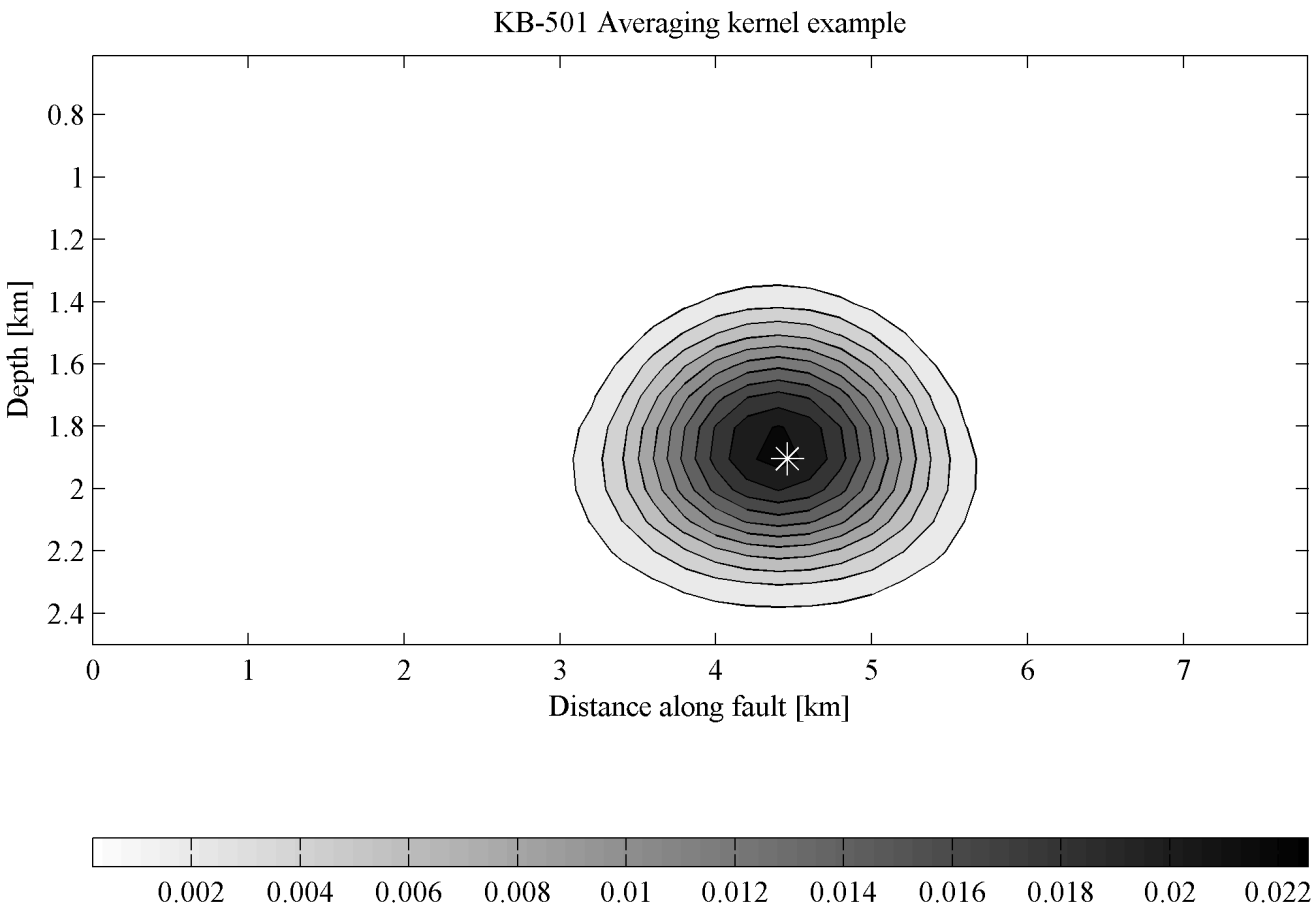
KB-501 Averaging kernel example
Depth [km]
0.8
1
1.2
1.4
1.6
1.8
2
2.2
2.4
0
1
2
3
4
5
6
7
Distance along fault [km]
0.002
0.004
0.006
0.008
0.01
0.012
0.014
0.016
0.018
0.02
0.022

Figure 8.

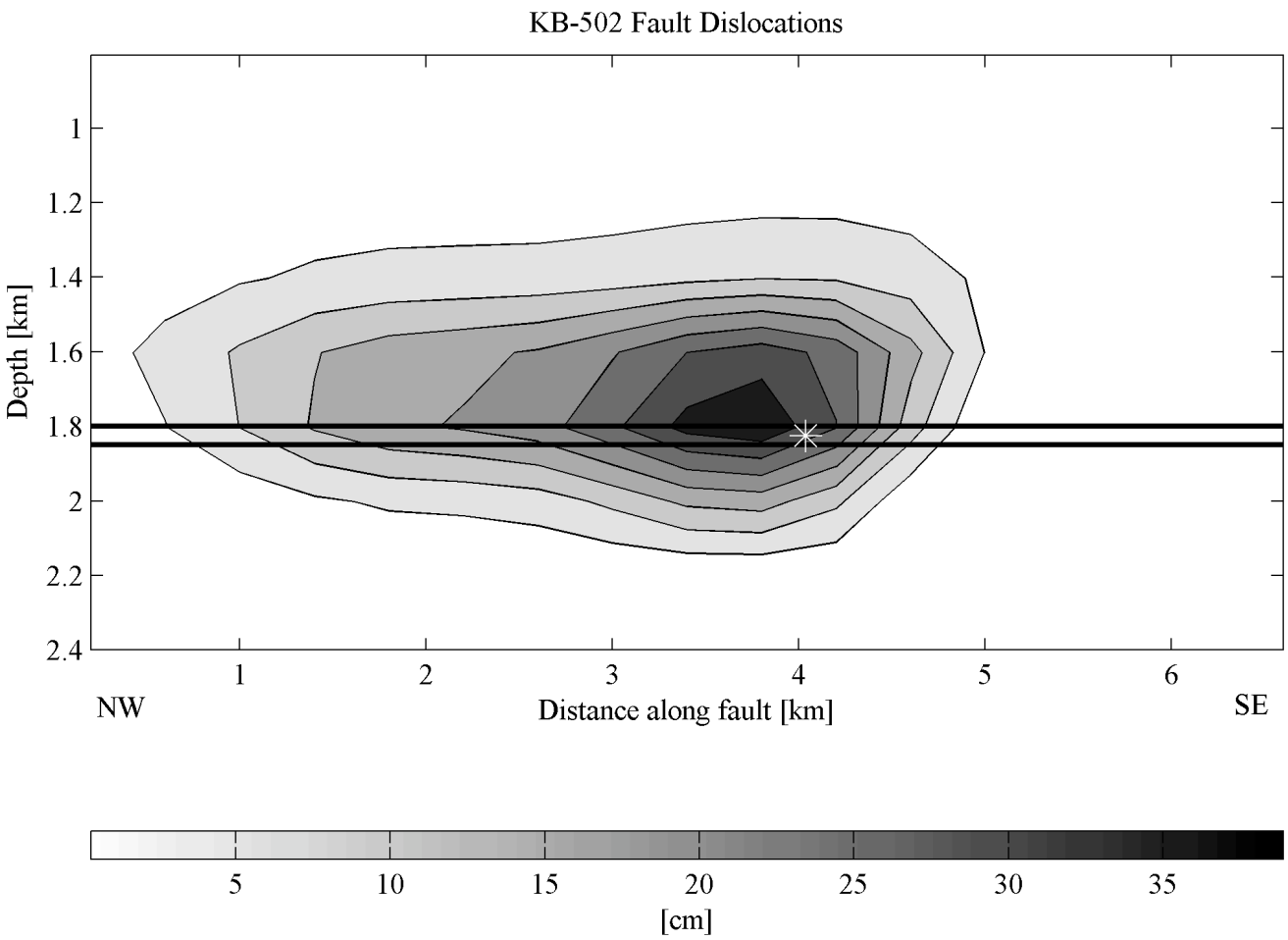
KB-502 Fault Dislocations
Depth [km]
1
1.2
1.4
1.6
1.8
2
2.2
2.4
1
2
3
4
5
6
NW
Distance along fault [km]
SE
5
10
15
20
25
30
35
[cm]

Figure 9a.

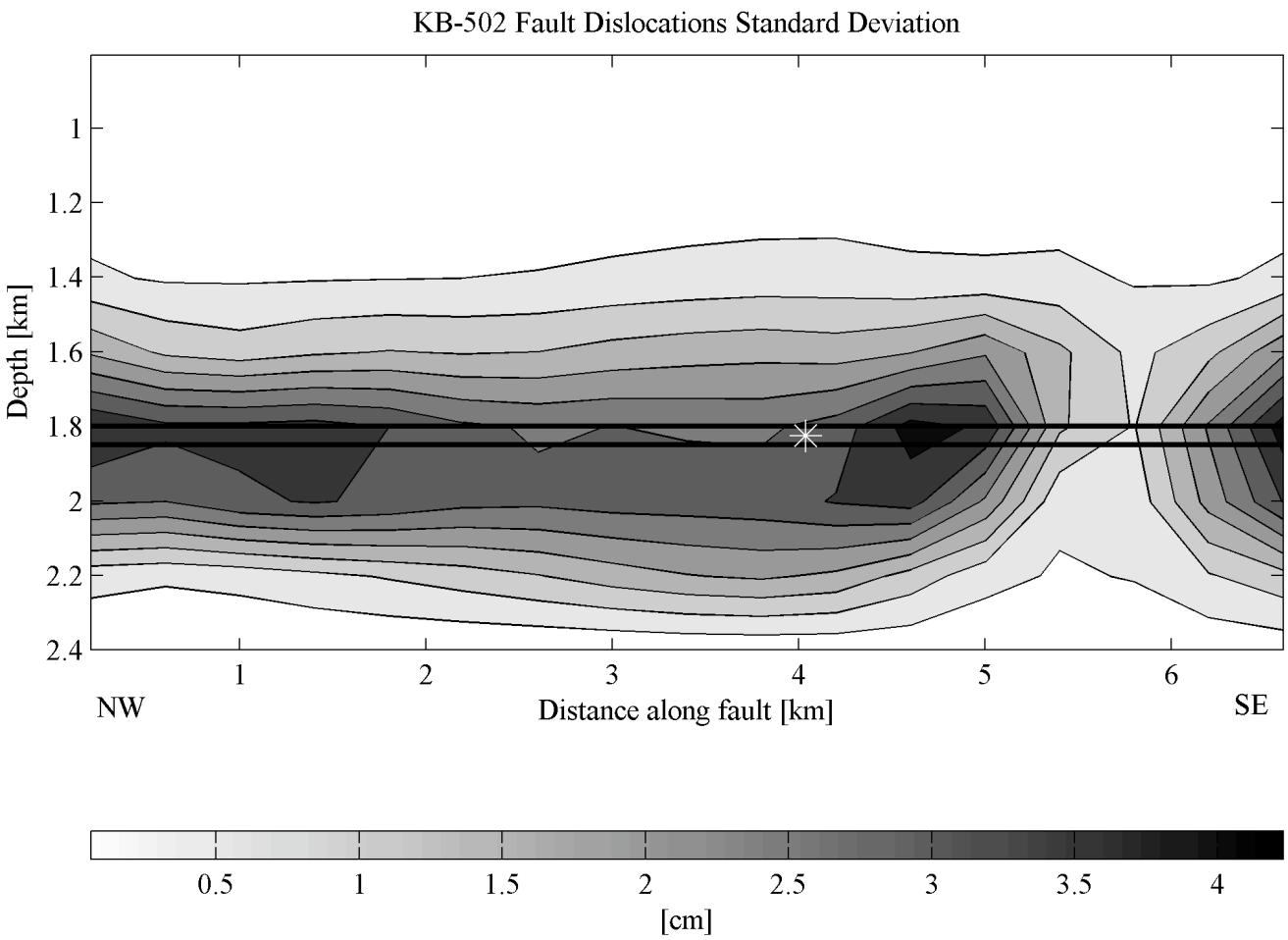
KB-502 Fault Dislocations Standard Deviation
Depth [km]
1
1.2
1.4
1.6
1.8
2
2.2
2.4
1
2
3
4
5
6
NW
Distance along fault [km]
SE
0.5
1
1.5
2
2.5
3
3.5
4
[cm]

Figure 9b.

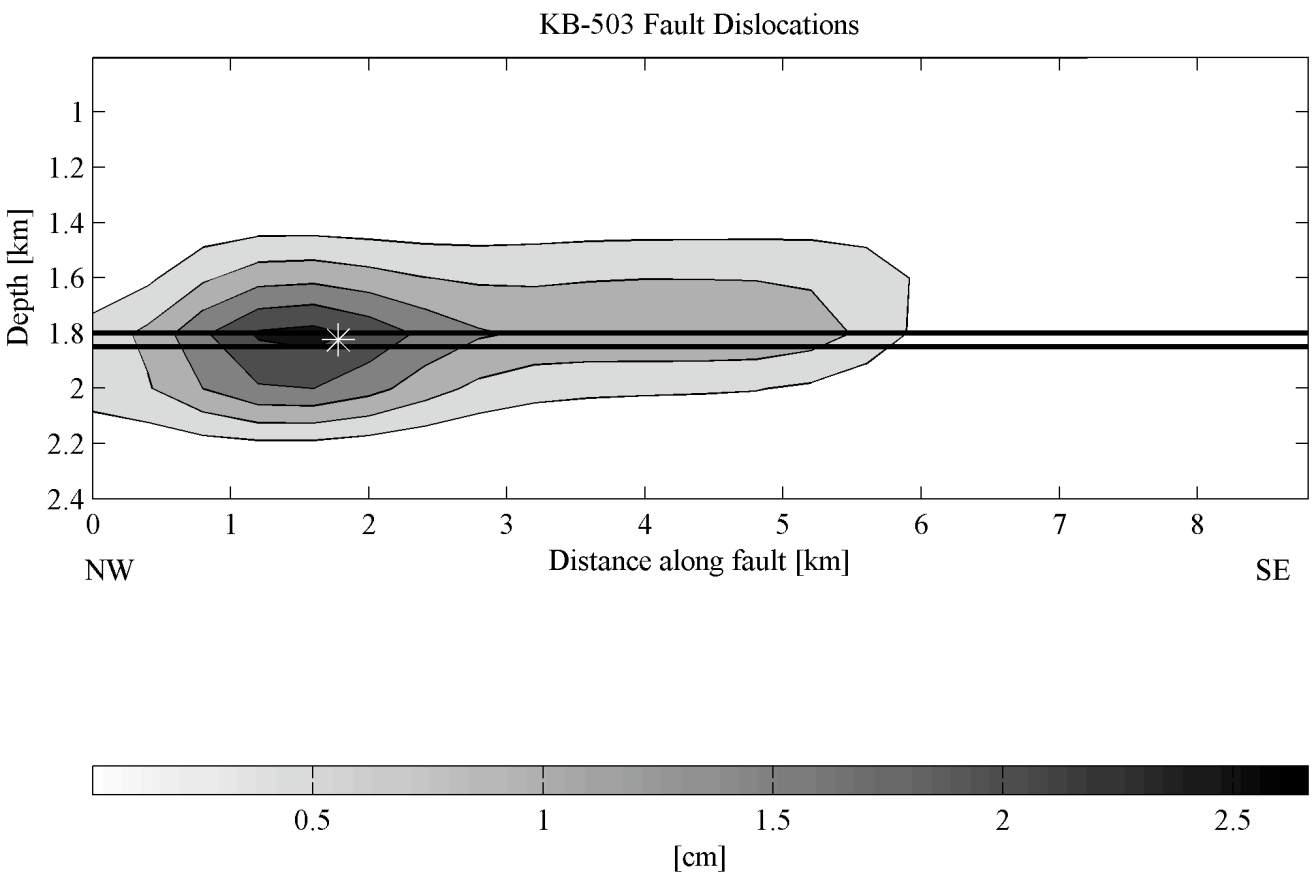
KB-503 Fault Dislocations
Depth [km]
1
1.2
1.4
1.6
1.8
2
2.2
2.4
0
1
2
3
4
5
6
7
8
NW
Distance along fault [km]
SE
0.5
1
1.5
2
2.5
[cm]

Figure 10a.

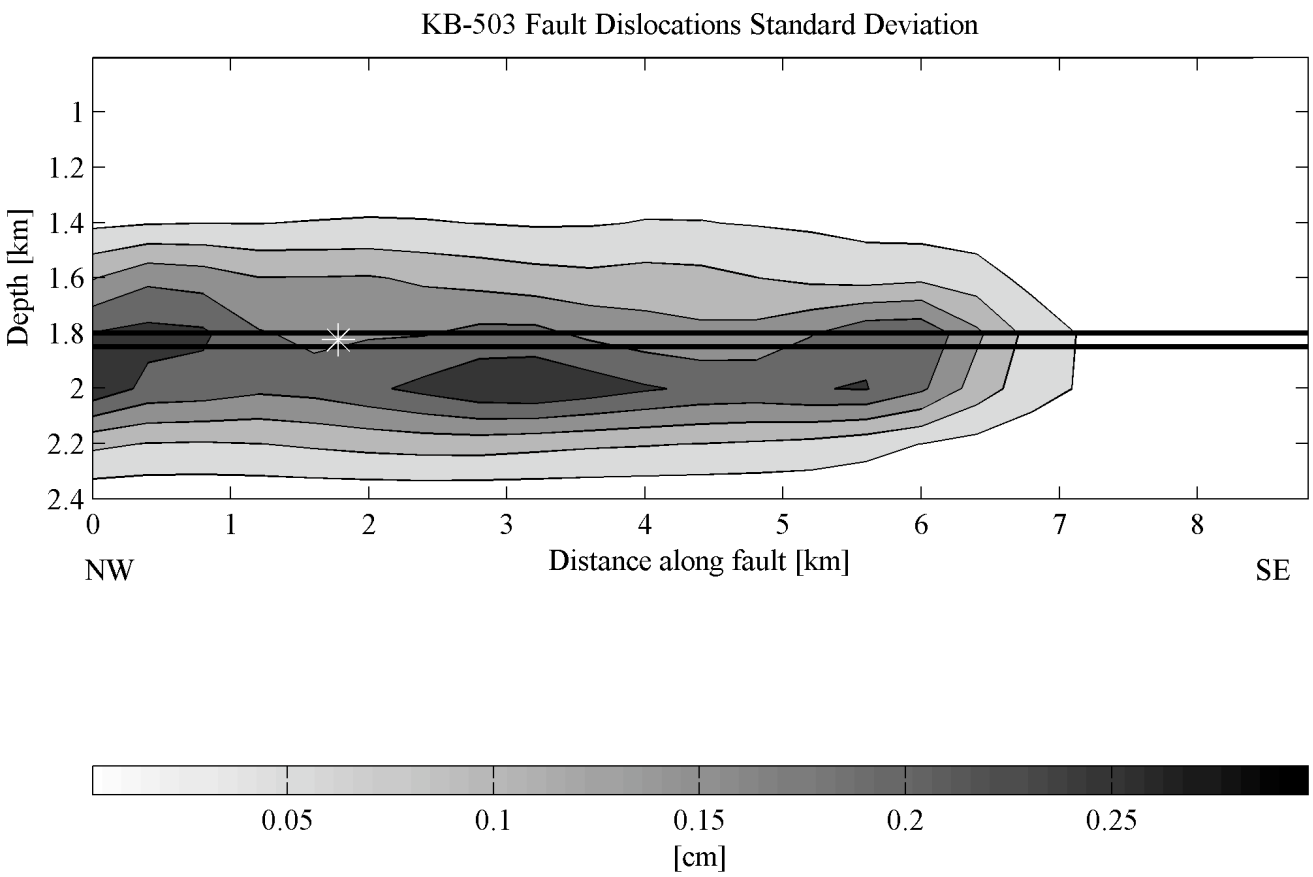
KB-503 Fault Dislocations Standard Deviation
Depth [km]
1
1.2
1.4
1.6
1.8
2
2.2
2.4
0
1
2
3
4
5
6
7
8
NW
Distance along fault [km]
SE
0.05
0.1
0.15
0.2
0.25
[cm]

Figure 10b.

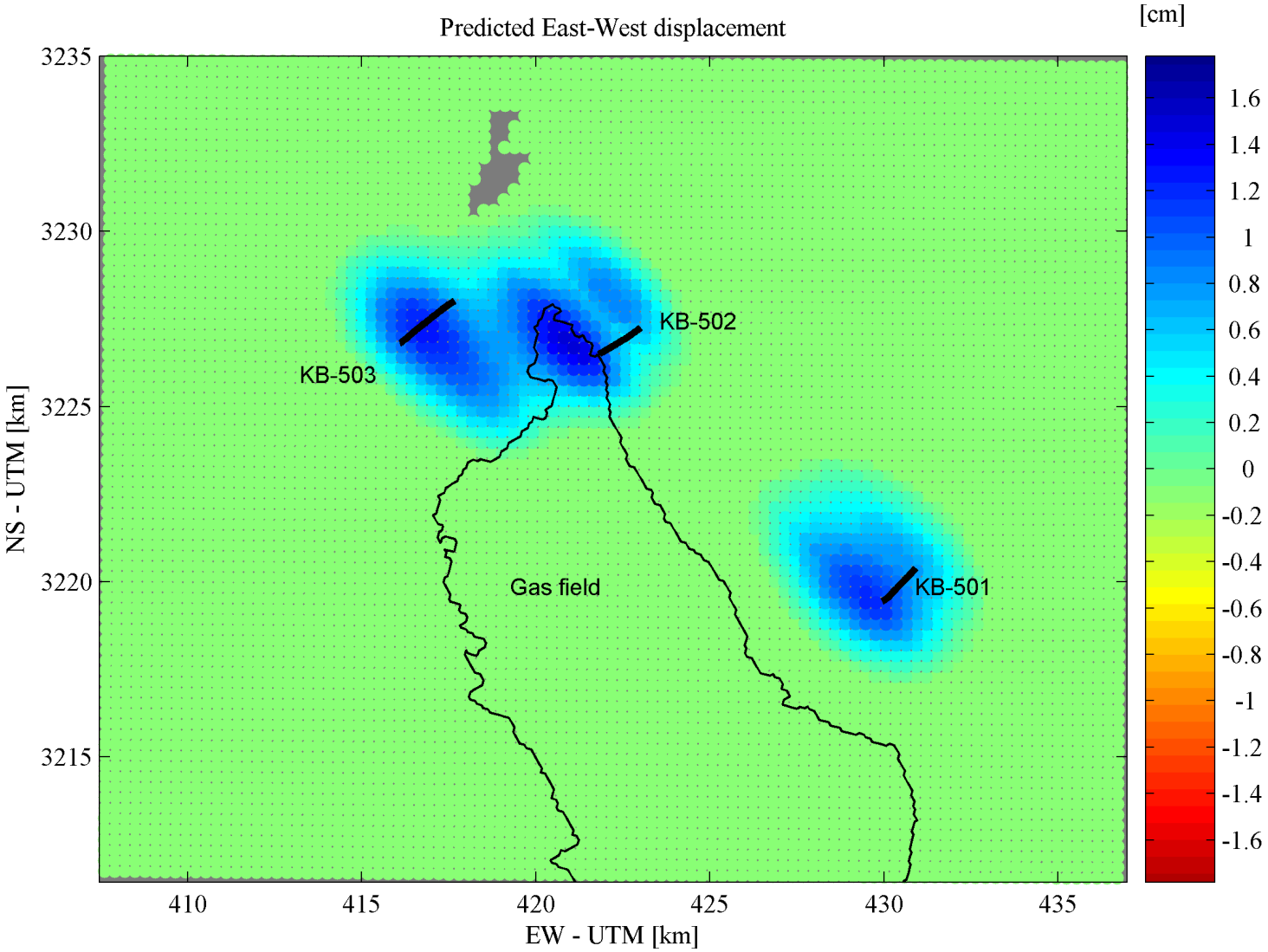
Predicted East-West displacement
[cm]
3235
3230
3225
3220
3215
NS - UTM [km]
410
415
420
425
430
435
EW - UTM [km]
KB-503
KB-502
KB-501
Gas field
1.6
1.4
1.2
1
0.8
0.6
0.4
0.2
0
-0.2
-0.4
-0.6
-0.8
-1
-1.2
-1.4
-1.6

Figure 11a.

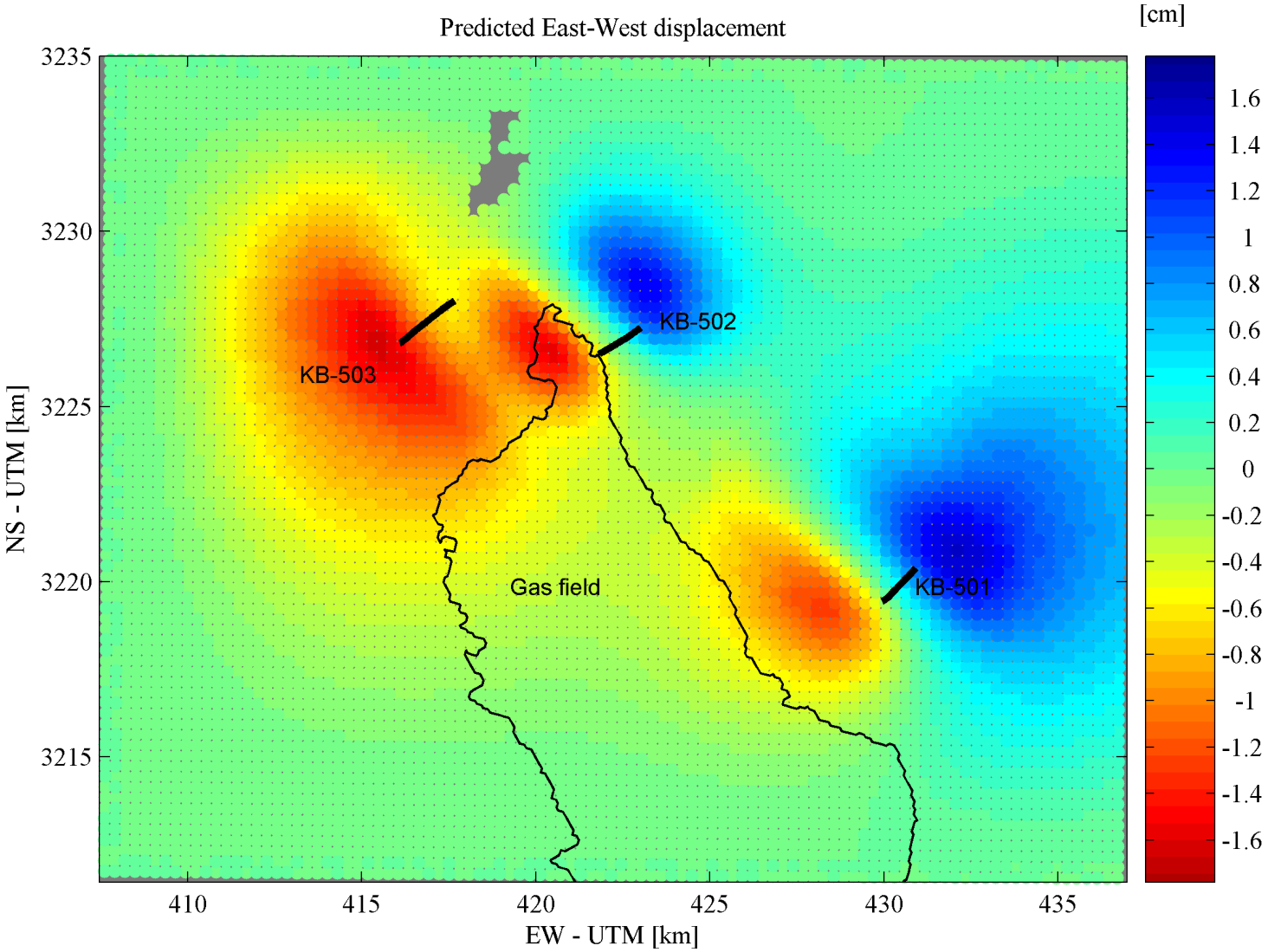
Predicted East-West displacement
[cm]
3235
3230
3225
3220
3215
NS - UTM [km]
410
415
420
425
430
435
EW - UTM [km]
KB-503
KB-502
KB-501
Gas field
1.6
1.4
1.2
1
0.8
0.6
0.4
0.2
0
-0.2
-0.4
-0.6
-0.8
-1
-1.2
-1.4
-1.6

Figure 11b.

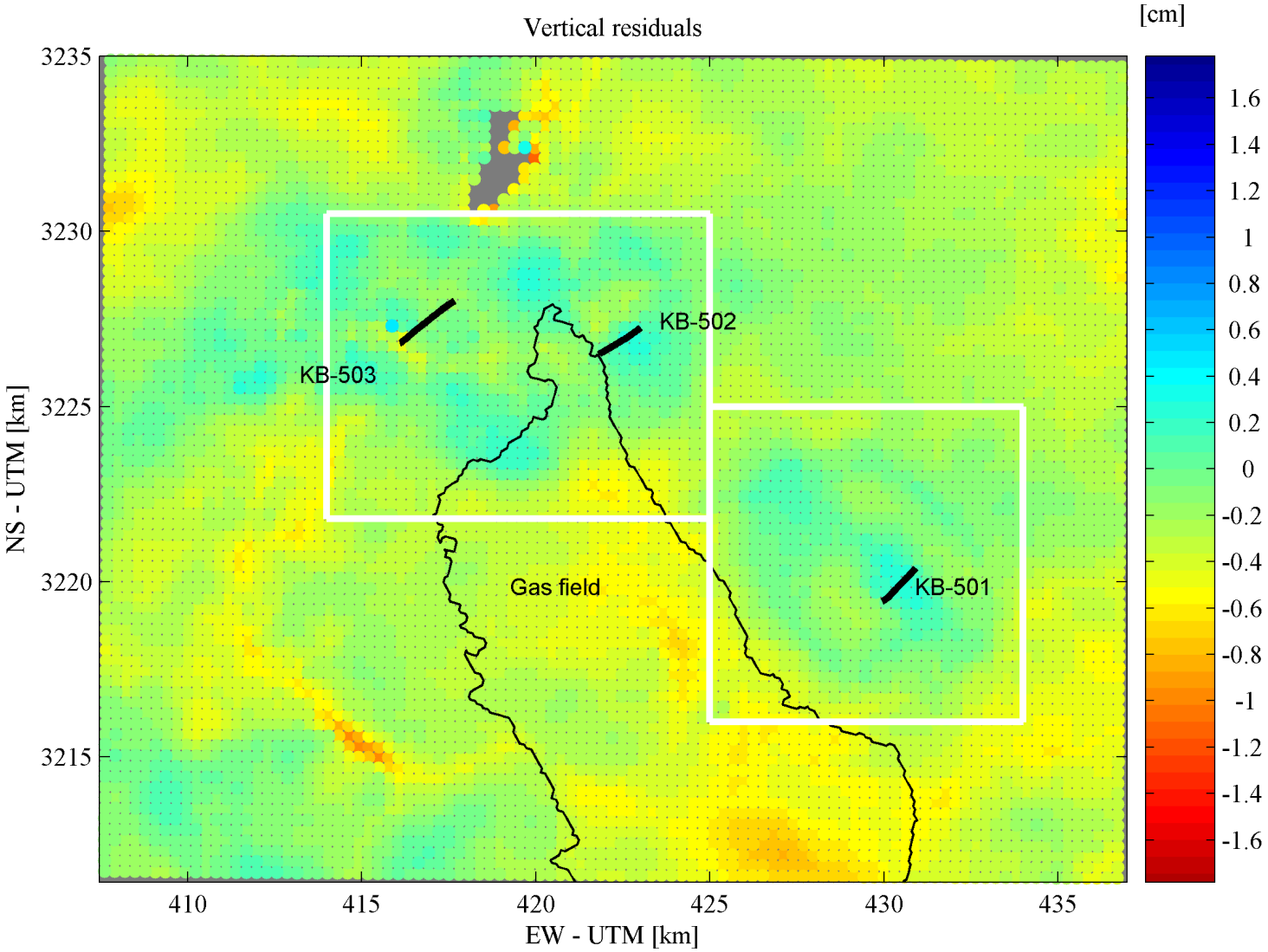
Vertical residuals
[cm]
3235
3230
3225
3220
3215
NS - UTM [km]
410
415
420
425
430
435
EW - UTM [km]
KB-503
KB-502
KB-501
Gas field
1.6
1.4
1.2
1
0.8
0.6
0.4
0.2
0
-0.2
-0.4
-0.6
-0.8
-1
-1.2
-1.4
-1.6

Figure 12a.

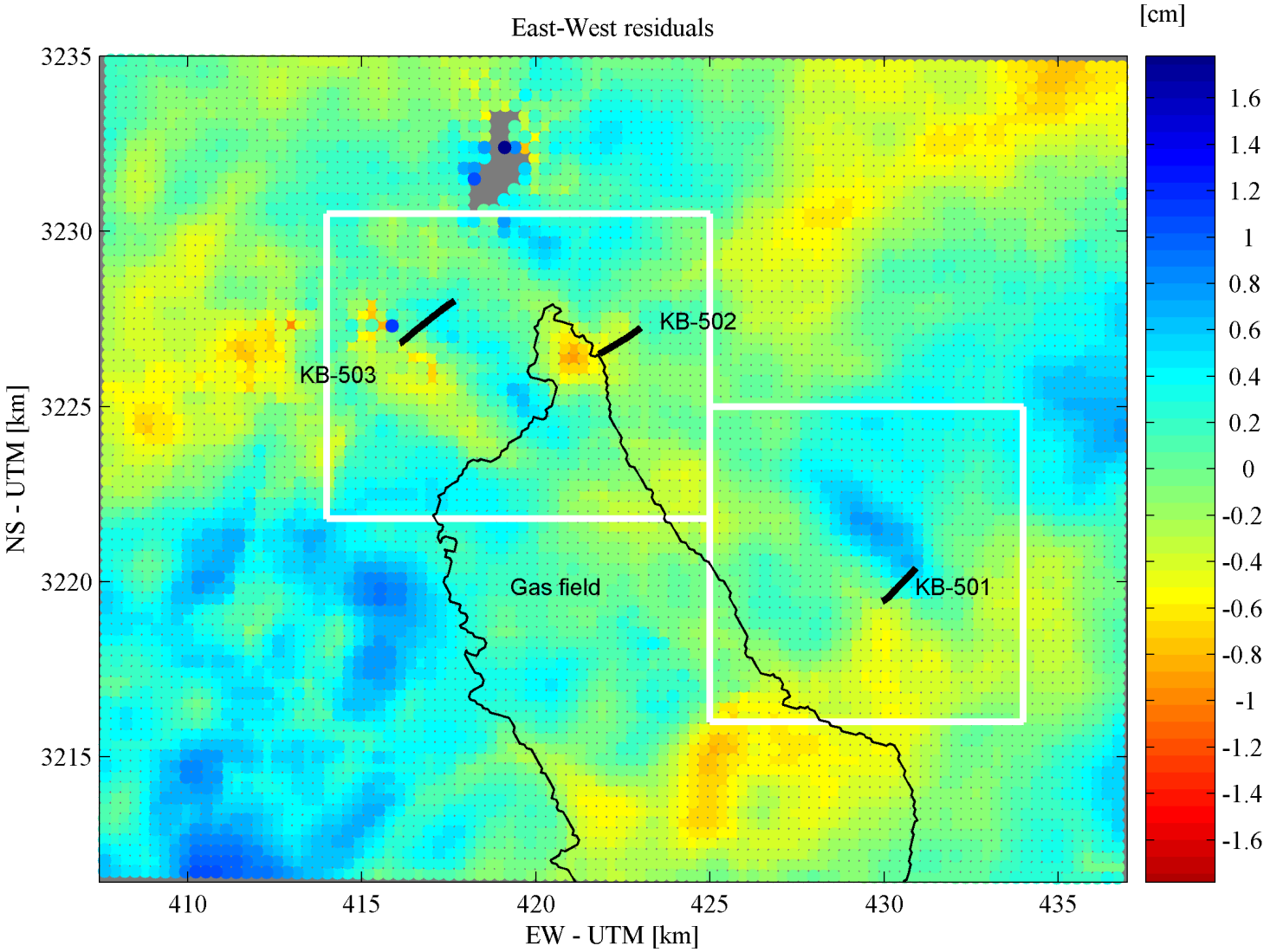
East-West residuals
[cm]
3235
3230
3225
3220
3215
NS - UTM [km]
410
415
420
425
430
435
EW - UTM [km]
KB-503
KB-502
KB-501
Gas field
1.6
1.4
1.2
1
0.8
0.6
0.4
0.2
0
-0.2
-0.4
-0.6
-0.8
-1
-1.2
-1.4
-1.6

Figure 12b.

DISCLAIMER

This document was prepared as an account of work sponsored by the United States Government. While this document is believed to contain correct information, neither the United States Government nor any agency thereof, nor The Regents of the University of California, nor any of their employees, makes any warranty, express or implied, or assumes any legal responsibility for the accuracy, completeness, or usefulness of any information, apparatus, product, or process disclosed, or represents that its use would not infringe privately owned rights. Reference herein to any specific commercial product, process, or service by its trade name, trademark, manufacturer, or otherwise, does not necessarily constitute or imply its endorsement, recommendation, or favoring by the United States Government or any agency thereof, or The Regents of the University of California. The views and opinions of authors expressed herein do not necessarily state or reflect those of the United States Government or any agency thereof or The Regents of the University of California.

Ernest Orlando Lawrence Berkeley National Laboratory is an equal opportunity employer.